

Diffuse interstellar bands in the H II region M17

Insights into their relation with the total-to-selective visual extinction R_V

M.C. Ramírez-Tannus¹, N.L.J. Cox², L. Kaper¹, and A. de Koter^{1,3}

¹ Anton Pannekoek Institute for Astronomy, University of Amsterdam, Science Park 904, 1098 XH Amsterdam, The Netherlands
e-mail: m.c.ramirez-tannus@uva.nl

² ACRI-ST, 260 Route du Pin Montard, Sophia Antipolis, France

³ Institute of Astronomy, KU Leuven, Celestijnenlaan 200D, 3001 Leuven, Belgium

August 31, 2018

ABSTRACT

Context. Diffuse interstellar bands (DIBs) are broad absorption features measured in sightlines probing the diffuse interstellar medium. Although large carbon-bearing molecules have been proposed as the carriers producing DIBs, their identity remains unknown. DIBs make an important contribution to the extinction curve; the sight line to the young massive star-forming region M17 shows anomalous extinction in the sense that the total-to-selective extinction parameter differs significantly from the average Galactic value and may reach values $R_V > 4$. Anomalous DIBs have been reported in the sight line towards Herschel 36 ($R_V = 5.5$), in the massive star-forming region M8. Higher values of R_V have been associated with a relatively higher fraction of large dust grains in the line of sight.

Aims. Given the high R_V values, we investigate whether the DIBs in sight lines towards young OB stars in M17 show a peculiar behaviour.

Methods. We measure the properties of the most prominent DIBs in M17 and study these as a function of $E(B - V)$ and R_V . We also analyse the gaseous and dust components contributing to the interstellar extinction.

Results. The DIB strengths in M17 concur with the observed relations between DIB equivalent width and reddening $E(B - V)$ in Galactic sight lines. For several DIBs we discover a linear relation between the normalised DIB strength EW/A_V and R_V^{-1} . These trends suggest two groups of DIBs: (i) a group of ten moderately strong DIBs that show a sensitivity to changes in R_V that is modest and proportional to DIB strength, and (ii) a group of four very strong DIBs that react sensitively and to a similar degree to changes in R_V , but in a way that does not appear to depend on DIB strength.

Conclusions. The DIB behaviour as a function of reddening is not peculiar in sight lines to M17. Also, we do not detect anomalous DIB profiles as seen in Herschel 36. DIBs are stronger, per unit visual extinction, in sight lines characterised by a smaller value of R_V , i.e. those sight lines that contain a relatively large fraction of small dust particles. New relations between extinction normalised DIB strengths, EW/A_V , and R_V support the idea that DIB carriers and interstellar dust are intimately connected. Furthermore, given the distinct behaviour of two groups of DIBs, different types of carriers do not necessarily relate to the dust grains in a similar way.

Key words. diffuse interstellar bands, dust, extinction, Star forming region, M17

1. Introduction

The nature of the carrier(s) of diffuse interstellar bands (DIBs) is one of the oldest mysteries in stellar spectroscopy. Over 400 DIBs have been observed in the optical wavelength range (e.g. Hobbs et al. 2009) and about a dozen DIBs have been detected in the near infrared (Geballe et al. 2011; Cox et al. 2014; Hamano et al. 2015). DIBs are thought to be large carbon-bearing molecules and may represent the largest reservoir of organic material in the Universe (Snow 2014). Laboratory experiments simulating interstellar conditions recently proposed C_{60}^+ as the carrier of the $\lambda 9577$ and $\lambda 9632$ DIBs (Campbell et al. 2015), but the vast majority of the DIBs remains unidentified. For a recent overview of DIBs, see Cami & Cox (2014).

DIBs measured in sight lines towards massive star forming regions are reported to behave differently compared to the average Galactic sight line. Hanson et al. (1997) noted that the DIBs observed in the direction of M17, over the extinction range of $A_V = 3 - 10$, show little change in spectral shape nor a significant increase in strength. They suggested that either the DIB

features are already saturated at a small value of the visual extinction A_V , or that the interstellar material local to M17, where the increased extinction is being traced, does not contain the DIB carriers. Dahlstrom et al. (2013) and Oka et al. (2013) detected anomalously broad DIBs at $\lambda\lambda 5780.5$, 5797.1 , and 6613.6 in the sight line to Herschel 36, an O star multiple system associated with the Hourglass nebula in the giant H II region M8 (Lagoon Nebula). The DIBs show an excess of absorption in the red wing of the profile; excited lines of CH and CH^+ are detected as well. Oka et al. (2013) interpret this observation as being caused by infrared pumping of rotational levels of relatively small molecules.

Sight lines towards massive star forming regions (Orion Trapezium region, Carina, M8) often show a high value of the total-to-selective extinction parameter R_V (see e.g. Cardelli et al. 1989; Fitzpatrick & Massa 2007). The common interpretation is that the value of R_V characterises the dust particle size distribution. Sight lines that include relatively many small dust particles display an extinction curve with a small value of R_V and produce stronger interstellar absorption at short (UV) wavelengths, and vice versa. Most Galactic sight lines have

$R_V \sim 3.1 \pm 0.3$ (Fitzpatrick & Massa 2007) and we refer to extinction curves with higher or lower values of R_V as anomalous.

The strongest feature in the extinction curve is the 2175 Å bump; although the carrier of this feature also remains unidentified, it is generally attributed to carbonaceous particles, either in the form of graphite, a mixture of hydrogenated amorphous carbon grains and polycyclic aromatic hydrocarbons (PAHs), or various aromatic forms of carbon (e.g. Mathis et al. 1977; Menella et al. 1998; Mishra & Li 2015). It is believed that the presence and strength of the bump depends on the metallicity of the environment as it appears slightly weaker in the LMC extinction curves, and it is essentially absent in the SMC extinction curve (Gordon & Clayton 1998; Misselt et al. 1999). Some sightlines towards the LMC (specifically the LMC 2 supershell near 30 Dor) and the SMC sight lines have small R_V values (~ 2.7 , Gordon et al. 2003). Remarkably, the one SMC line of sight that exhibits normal strength DIBs (and CH) shows Galactic-type dust extinction and includes the 2175 Å extinction feature (Ehrenfreund et al. 2002; Welty et al. 2006; Cox et al. 2007). Furthermore, Galactic sight lines that are SMC-like show very weak DIBs per unit reddening (Snow et al. 2002; Cox et al. 2007).

If the carriers of the DIBs and those of the 2175 Å bump are produced from the same initial dust through the same physical process, or if the DIB carriers originate from the fragmentation of the 2175 Å bump carriers, one would expect them to be related. More recently Xiang et al. (2011) studied the relation between DIBs and the 2175 Å bump in detail. They collected 2175 Å bump and DIB strength measurements, from the literature, towards 84 interstellar sightlines for eight DIBs and found no significant correlation between the two. They explain the lack of a correlation by hypothesising that DIB carriers correspond to the smallest, free-flying PAH molecules and ions, while the 2175 Å carriers correspond to the larger or clustered PAHs.

In Ramírez-Tannus et al. (2017, hereafter Paper I) we studied a sample of young massive (pre-)main-sequence stars in the giant H II region M17 located at a distance of $1.98^{+0.14}_{-0.12}$ kpc (Xu et al. 2011). We obtained optical to near-infrared VLT/X-shooter spectra and derived the extinction parameters by modelling the spectral energy distribution. The sight lines are characterised by anomalous extinction (R_V in the range 3.3 to 4.6 and A_V between 5 and 14 mag). M17 is one of the most luminous star-forming regions in the Galaxy with a luminosity of $3.6 \times 10^6 L_\odot$ (Prinzano et al. 2007). It contains about 16 O stars and more than 100 B stars; its age is ≤ 1 Myr (Hanson et al. 1997; Hoffmeister et al. 2008; Broos et al. 2007; Povich et al. 2009, Paper I).

In this paper we present a detailed analysis of the DIBs in eight sight lines to M17, taking into account the anomalous extinction observed in this region ($R_V > 3.1$). Earlier work hinted at the peculiar behaviour of the DIBs in these sight lines (Hanson et al. 1997) and we investigate whether the DIB properties are somehow related to the extinction caused by dust. Such a relation may shed new light on the physical and chemical nature of the DIB carriers.

The paper is organised as follows: in the next section we briefly describe the data set and reduction procedure, and in Section 3 we characterise the interstellar extinction in the direction of M17, both the gaseous and the dust component. In Section 4 the DIB properties are presented. Subsequently, we compare the DIB properties to those observed in other Galactic sight lines (Section 5). In Section 6 we address the observed dependence of the DIBs in M17 on the value of R_V . In Section 7 we discuss the results in the context of the anomalous extinction and the prop-

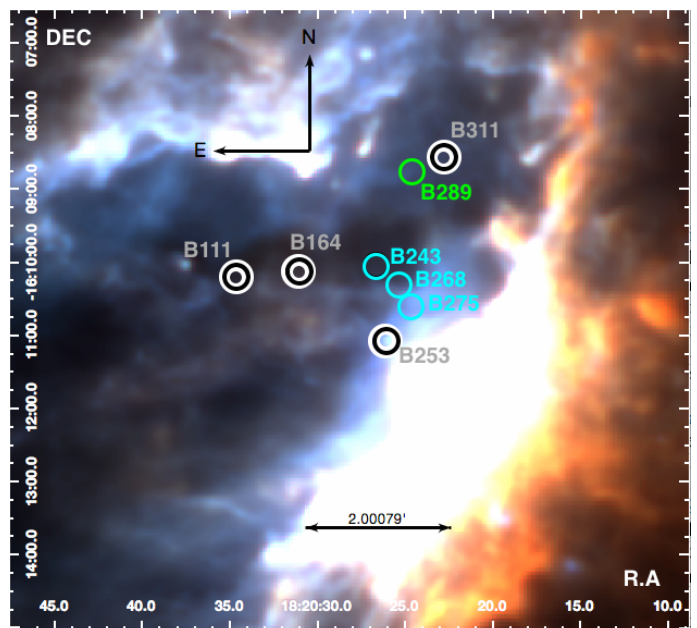


Fig. 1. Far-infrared colour composite image of M17 based on *Herschel* PACS data. Blue: 70 μm , green: 100 μm , and red: 160 μm . The sources with circumstellar disks are shown in blue, the ones with IR excess longward of 2.5 μm in green and the "naked" OB stars in black. We do not observe an obvious trend in extinction properties with the location in the region.

erties of the interstellar dust. In the last section we summarise our conclusions.

2. X-shooter observations

We have obtained VLT/X-shooter (300 – 2500 nm) (Vernet et al. 2011) spectra of 11 (pre-)main sequence (PMS) stars ranging in mass from 6 to 20 M_\odot . We selected this sample from the list of candidate massive PMS stars reported by Hanson et al. (1997) and we determined their stellar and extinction properties, which are presented in Paper I. The location of the observed targets in M17 is shown in Fig. 1. With the exception of Fig. 10, throughout this paper we color-code the M17 sightlines according to the properties of the stellar spectral energy distributions. The blue circles represent the sight lines towards objects with circumstellar disks (gas+dust disks), the green triangles towards stars with IR excess longwards of 2.5 μm (dusty disks), and the black squares towards OB stars without detected circumstellar material. We reduced the spectra using the X-shooter pipeline (Modigliani et al. 2010) version 2.7.1 running under the ESO Reflex environment (Freudling et al. 2013) version 2.8.4. The flux calibration was obtained using spectrophotometric standards from the ESO database. We then scaled the NIR flux to match the absolutely calibrated VIS spectrum. The telluric correction was performed using the software tool *molecfit* v1.2.0¹ (Smette et al. 2015; Kausch et al. 2015). The data reduction and analysis are described in detail in Paper I.

We calculated the stellar properties of the objects with visible photospheres by fitting FASTWIND models (Puls et al. 2005; Rivero González et al. 2012) and obtained the total extinction in the V-band, A_V , and the visual-to-selective extinction ratio, R_V , by fitting the flux calibrated X-shooter spectra

¹ <http://www.eso.org/sci/software/pipelines/skytools/molecfit>

to Castelli & Kurucz (2004) models. The spectral type and extinction properties presented in Paper I are listed in Table 1. In this paper we compare the results obtained in Paper I where we use the Cardelli et al. (1989) extinction law to deredden the flux calibrated spectra with results obtained by using the Fitzpatrick & Massa (2007) parameterisation of the extinction curve. We also compare the extinction parameters obtained by SED fitting with that derived from the colour excess $E(B-V)$ (see Section 3). We list the R_V value obtained from Eq. 1; for objects with a near-infrared excess (i.e., a circumstellar disk: B243, B268, and B275) we iterated this equation starting with $A_K = 0$. In this way we obtain an estimate of the K -band extinction A_K , and thus a measure of the near-infrared excess (Section 3).

3. Extinction towards M17

By dereddening the SEDs of a dozen OB stars Hanson et al. (1997) detected a significant spread in both visual extinction A_V (3–15 mag) and in total-to-selective extinction R_V (2.8–5.5). They point out that the nebulosity disappears at the centre of the region and that the highest extinction is measured at the edges of this void. They also note that the DIB strengths (4430 and 4502 Å) do not show a significant increase even though the visual extinction towards these objects varies from 3–10 mag. Earlier studies indicated that $R_V = 4.9$ (Chini & Kruegel 1983) based on NIR photometry (but without knowledge of the spectral types), and $R_V = 3.3$ using the maximum polarisation relation for R_V (Schulz et al. 1981). Hoffmeister et al. (2008) concluded that the foreground extinction, with $A_V \sim 2$ mag and $R_V = 3.1$, differs from the extinction local to M17 for which they measure $R_V = 3.9 \pm 0.2$.

3.1. Dust extinction

In Paper I we constructed the spectral energy distribution (SED) of the stars by dereddening the X-shooter spectrum, as well as the available photometric data. In order to deredden the spectrum we used the Cardelli et al. (1989) extinction law. We then constrained A_V and R_V towards the objects in M17 by fitting the slope of their SED in the photospheric domain (400–820 nm) to Castelli & Kurucz models² (Kurucz 1993; Castelli & Kurucz 2004) corresponding to the spectral type reported in Table 1.

The obtained values for R_V range from 3.3 to 4.7 and A_V varies from ~6 to ~15 mag. We do not find a significant correlation of the extinction properties with the position of the stars in the star forming region. Cardelli et al. (1989) mention that their parameterisation of the extinction law becomes inaccurate when R_V is large. As an example they refer to the sight line to Herschel 36.

As we know the spectral type of the targets, we can compare the value of the colour excess $E(B-V) \equiv A_V/R_V$ measured by fitting the SED with the value obtained directly by comparing the observed magnitudes to the intrinsic ones ($E(B-V) = (B-V) - (B-V)_0$). We adopt an error of 0.1 mag in $E(B-V)$ in order to account for the uncertainty in the spectral classification and the photometric errors. For the main sequence stars we took the value of B_0 and V_0 from Pecaut & Mamajek (2013). For the giants we used the calibration in Wegner (2000, 2014). The comparison is shown in the left panel of Fig. 2. The value of $E(B-V)$ derived from the SED fitting method is systematically higher than the one obtained directly from the observed and the

intrinsic colours. The $E(B-V)$ values obtained with the SED fitting method and the Fitzpatrick (1999) extinction law are closer to those obtained directly from the colors and we do not observe a systematic trend. Apparently, we underestimate the value of R_V with the SED fitting method and the Cardelli et al. (1989) extinction law.

In order to investigate this further, we calculated R_V using the relation reported in Fitzpatrick & Massa (2007):

$$R_V = -0.26 + 1.19 \frac{E(V-K)}{E(B-V)} = -0.26 + 1.19 \frac{A_V - A_K}{A_B - A_V} \quad (1)$$

Given that this relation uses the K -band magnitude, it implicitly assumes that the target's SED does not include an IR excess or, alternatively, that this is corrected for. In the case of the three objects with circumstellar disks (blue dots in the plots), we calculated R_V by iterating Eq. 1. With $A_V = V - V_0$ and $E(B-V) = (B-V) - (B-V)_0$, we started assigning a value of $A_K = 0$ and calculated R_V from this equation; we then used Fitzpatrick's extinction law to calculate A_K with the obtained R_V and repeated this process until the values for both R_V and A_K converged. We arrive at $R_V = 4.6, 3.3$ and 3.1 for B243, B268, and B275, respectively³. The comparison between the colour excess calculated with Fitzpatrick's extinction law and the one based on the observed and intrinsic colour is shown in the right panel of Fig. 2. From the figure it is clear that the values obtained using these two methods agree within the errors. We note that, in the case of objects with near-IR excess, these two methods are not completely independent, because we used the values based on the observed and intrinsic colour as initial guess to iterate Eq. 1.

We conclude that with the method used in Paper I, where the Cardelli et al. (1989) extinction law is used to deredden the SEDs for sightlines with high R_V , we underestimate the value of this parameter. Furthermore, we observe that the values for A_V obtained with the three methods agree with each other. This means that we do not make a significant error when calculating the luminosity of the objects in Paper I.

We do not find a systematic difference between the values obtained for objects with circumstellar gaseous disks (blue dots), only dusty disks (green triangle), and naked OB stars (black squares).

In the remainder of this paper we will adopt the values of $A_V = V - V_0$, $E(B-V) = (B-V) - (B-V)_0$ and R_V derived from Eq. 1.

3.2. The gaseous component of the extinction

The Ca II, Na I, and K I interstellar lines are shown in Figure 3; we have over plotted the DIB at 5780 Å. The velocities have been corrected into the barycentric rest frame. In Table 2 we list the local standard rest frame (LSR) velocity measured for each of the lines. These radial velocities are consistent with interstellar absorption at distances of 1.3–2.2 kpc based on Galactic rotation models by Reid et al. (2009). We observe hardly any difference from one sight line to the other. The atomic lines are mostly unresolved at the moderate X-Shooter spectral resolution of $R \sim 11000$. Although inconclusive regarding the exact distribution of gas in these lines-of-sight these data indicate the main gaseous absorption features are associated with M17 at ~2 kpc.

³ With this accurate measurement of the extinction properties we calculate K -band excesses of 2 to 3 magnitudes for B243, B268, and B275. In a forthcoming paper (Poorta et al., *in prep.*) we investigate the physical properties of the circumstellar disks that cause the measured K -band excess.

² Table 2 in http://www.stsci.edu/hst/observatory/crds/castelli_kurucz_atlas.html

Table 1. Extinction properties measured in the sight lines towards M17. The first column lists the star’s identifier, the second the spectral type as reported in [Paper I](#). The third, fourth, and fifth columns show the B , V , and K -band magnitudes, respectively. Columns 6, 8, and 10 list the extinction parameters (R_V , A_V , and $E(B - V) = A_V/R_V$) derived by fitting the spectral energy distribution to Kurucz models. We list the R_V and A_K values derived using Eq. 1 (see Section 3 for more information on objects with circumstellar disks) in columns 7 and 12. Column 9 lists the V -band excess A_V , and column 11 shows the colour excess $(B - V) - (B - V)_0$, where the intrinsic colour $(B - V)_0$ is taken from [Pecaut & Mamajek \(2013\)](#) and [Wegner \(2000, 2014\)](#).

Identifier	Sp.type	B mag	V mag	K^a mag	R_V SED	R_V Fitzp.	A_V SED (mag)	A_V $V - V_0$	$E(B - V)$ SED	$E(B - V)$ $(B - V) - (B - V)_0$	A_K mag
B111	O4.5 V	12.24 ^b	11.21 ^b	7.475	3.7 ^{+0.4} _{-0.3}	3.86	5.4 ^{+0.4} _{-0.3}	5.17	1.47 ± 0.13	1.35	0.50
B164	O6 Vz	16.85 ^c	15.41 ^c	8.758	3.8 ^{+0.3} _{-0.3}	4.87	8.3 ^{+0.4} _{-0.5}	9.03	2.2 ± 0.10	1.76	1.44
B215	B0-B1 V	–	16.10 ^d	10.00	4.1 ^{+0.2} _{-0.2}	–	7.6 ^{+0.3} _{-0.3}	8.17	1.85 ± 0.06	–	1.15
B243	B8 V	19.10 ^c	17.80 ^c	9.544	4.7 [†] _{-0.8}	4.64	8.5 [†] _{-1.0}	6.52	1.82 ± 0.22	1.41	0.72
B253	B3-B5 III	17.11 ^c	15.74 ^c	10.31	4.1 ^{+0.1} _{-0.2}	4.29	6.5 ^{+0.1} _{-0.2}	6.22	1.59 ± 0.06	1.52	0.41
B268	B9-A0	18.40 ^c	17.10 ^c	9.494	4.6 [†] _{-0.8}	3.47	8.1 [†] _{-1.0}	4.71	1.75 ± 0.25	1.34	0.52
B275	B7 III	17.02 ^c	15.55 ^c	7.947	3.8 ^{+0.7} _{-0.8}	3.35	6.7 ^{+0.8} _{-1.0}	5.44	1.77 ± 0.26	1.59	0.61
B289	O9.7 V	16.97 ^c	15.55 ^c	9.178	3.7 ^{+0.4} _{-0.5}	4.80	8.3 ^{+0.6} _{-0.8}	8.13	2.23 ± 0.17	1.73	0.78
B311	O8.5 Vz	14.99 ^c	13.69 ^c	8.884	3.3 ^{+0.3} _{-0.3}	4.00	6.1 ^{+0.4} _{-0.4}	6.51	1.85 ± 0.11	1.62	0.71
B331	late-B	–	20.10 ^c	8.946	4.6 ^{+0.5} _{-0.5}	–	13.3 ^{+0.9} _{-0.9}	–	2.89 ± 0.13	–	–
B337	late-B	–	–	9.343	3.7 ^{+0.4} _{-0.5}	–	8.3 ^{+0.6} _{-0.8}	–	3.66 ± 0.25	–	–

^a 2MASS catalogue ([Cutri et al. 2003](#)).

^b AAVSO Photometric all sky survey (APASS) catalog: <https://www.aavso.org/apass>

^c [Chini et al. \(1980\)](#)

^d [Hoffmeister et al. \(2008\)](#)

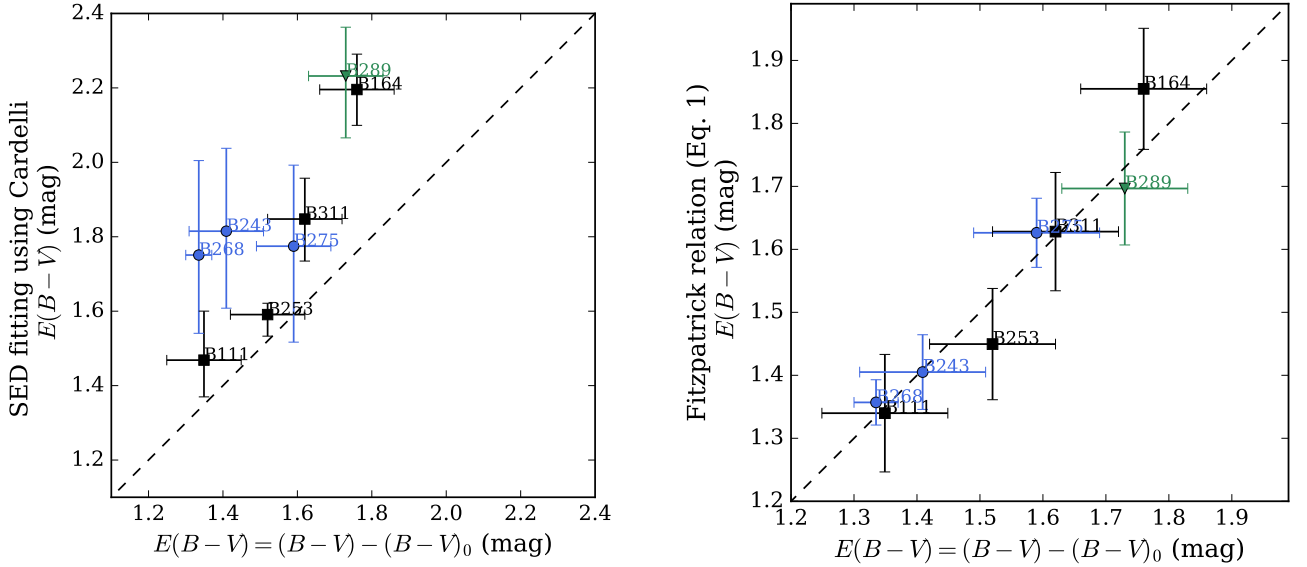


Fig. 2. *Left:* The colour excess $E(B - V)$ derived from SED fitting (A_V/R_V , [Paper I](#)) versus the value obtained using the observed and the intrinsic colour $(B - V)_0$; the latter is based on the spectral type reported in [Paper I](#). *Right:* The colour excess obtained from A_V/R_V , where R_V is estimated using Eq. 1 in [Fitzpatrick & Massa \(2007\)](#), versus the value obtained by using the observed and the intrinsic colour, as in the left panel. Now the discrepancy between these two values has been removed, demonstrating that the [Cardelli et al. \(1989\)](#) parameterisation underestimates the value of R_V in these sight lines. The blue circles represent the sight lines towards objects with circumstellar disks, the green triangles towards stars with dusty disks, and the black squares towards OB stars.

From 3D dust extinction maps ([Drimmel et al. 2003](#)) we find that the predicted visual extinction up to 1.8 kpc in the direction of M17 (i.e. in the foreground) corresponds to roughly 2 mag (or $E(B - V) = 0.65$ mag for a canonical value $R_V = 3.1$),

which is consistent with [Hoffmeister et al. \(2008\)](#). From the $E(B - V)$ versus distance towards M17 plot obtained via the on-line tool STILISM⁴ by [Capitanio et al. \(2017\)](#) we obtain a value

⁴ <http://stilism.obspm.fr>

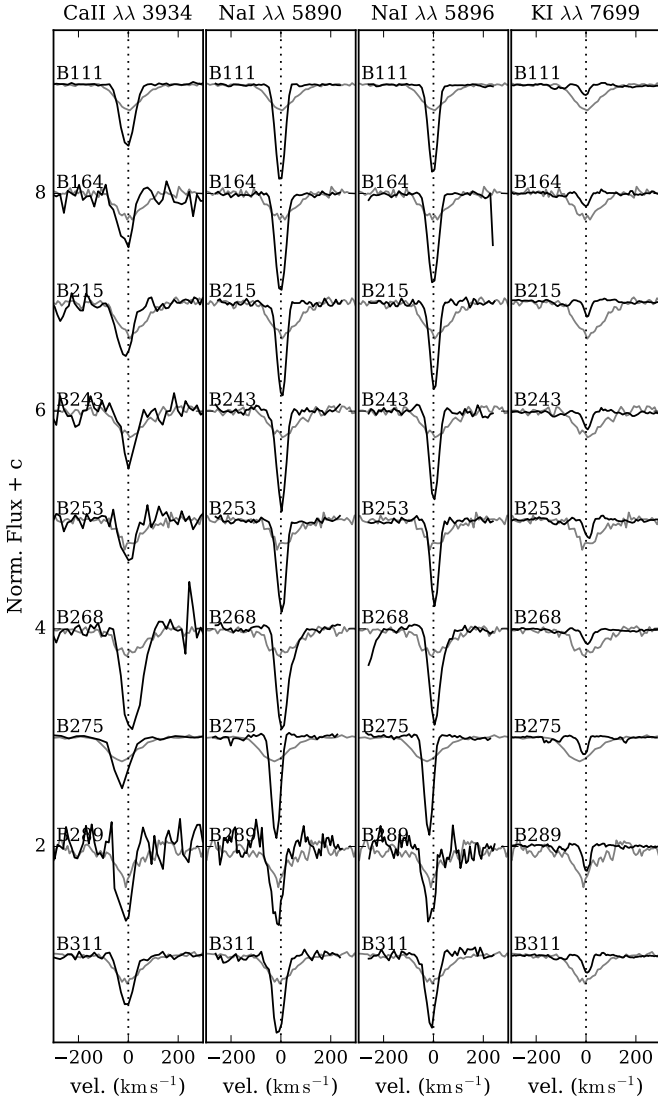


Fig. 3. Velocity profiles for the Ca II, Na I, and K I lines (black). We have over plotted the DIB at 5780 Å for reference (grey). The velocities are in the barycentric rest frame. The interstellar (gaseous) absorption is very similar comparing one sight line to the other and is likely due to a single cloud.

of $E(B - V) = 0.78$ mag at the distance M17, which is in line with our result. This plot shows that there are diffuse clouds in the foreground to the local gas and dust associated with the M17 region.

4. Diffuse interstellar bands

In this section we provide an overview of the DIB properties measured in the sight lines to the young OB stars in the star forming region M17. We analysed the nine strongest DIBs present in the spectra obtained by the UVB and VIS arms of X-shooter (at 4430, 5780, 5797, 6196, 6284, 6379, 6614, 7224, and 8620 Å). We also included the NIR DIBs at 11797 and 13176, first reported by Joblin et al. (1990), and the one at 15268 (Geballe et al. 2011; Cox et al. 2014). The DIB equivalent width (EW) and full width at half maximum (FWHM) are listed in Table 3. The first column corresponds to the central wavelength of the

Table 2. Local standard rest frame (LSR) radial velocities obtained from a Gaussian fit to the Ca II, Na I, and K I interstellar lines in each line of sight.

Identifier	Ca II	Na I	Na I	K I
$\lambda\lambda$	3933.66	5889.95	5895.92	7698.974
	km s ⁻¹	km s ⁻¹	km s ⁻¹	km s ⁻¹
B111	9.3 ± 0.4	11.3 ± 0.2	12.1 ± 0.2	–
B164	0.8 ± 3.5	12.6 ± 0.3	12.7 ± 1.3	10.4 ± 1.3
B215	-1.2 ± 2.3	16.8 ± 0.3	16.7 ± 0.3	18.9 ± 1.0
B243	16.6 ± 13.5	15.4 ± 0.4	15.7 ± 0.5	18.2 ± 1.4
B253	10.7 ± 6.1	16.2 ± 0.4	18.6 ± 0.3	22.4 ± 1.1
B268	28.8 ± 2.2	21.7 ± 0.8	20.4 ± 1.4	19.6 ± 1.5
B275	-13.2 ± 1.0	-6.1 ± 0.4	-5.1 ± 0.3	5.1 ± 1.1
B289	-9.1 ± 5.2	-11.3 ± 1.6	-9.9 ± 1.7	–
B311	7.3 ± 1.1	4.1 ± 0.7	4.6 ± 0.8	–

DIBs, the top values show the FWHM in nm, and the bottom values show the EW measurements in (mÅ).

We also detect the 9577 and 9632 DIBs whose carrier has recently been identified in the laboratory to be the C_{60}^+ molecule (Campbell et al. 2015). The FWHM and EW of these two DIBs are displayed in rows 10 and 11 of Table 3.

We searched for the presence of CH^+ and CH at 4232, 4300 Å but given the signal to noise of our data at such blue wavelengths, we were not able to detect these molecules in the X-shooter spectra.

4.1. DIB strengths and widths

The EW was measured by integrating the flux of each DIB within the boundaries shown in Appendix A. The error in the EW was calculated following the method described in Vos et al. (2011): $\sigma_{EW} = \sqrt{2\Delta\lambda\delta\lambda}/SNR$, where $\Delta\lambda$ is the integration range and $\delta\lambda$ is the spectral dispersion. The real errors might be larger due to unknown systematic uncertainties, particularly regarding the continuum normalisation. The SNR was measured in the shaded region shown in Appendix A. The FWHM ($= 2\sqrt{2\ln 2}\sigma$) of each DIB was measured by fitting a Gaussian function to the absorption lines.

4.2. Correlation between EW(6196) and EW(6613)

In order to check the consistency of the measurements we show our data, together with literature data, for the strongly correlated DIBs at 6614 and 6696 Å in Fig. 4 (McCall et al. 2010; Królowski et al. 2016). The dashed line shows a linear fit to the data by McCall et al. (2010) and the grey region shows the 2σ error on the fit. The measured ratios are in agreement with the trend observed in other Galactic sight lines.

4.3. C_{60}^+ bands

We measured the C_{60}^+ bands at 9577 and 9632 Å. The EW of the 9577 DIB increases roughly with A_V . B331 is an outlier with relatively weak 9577 and 9632 Å DIBs. The average measured 9632/9577 ratio is 1.1 which is higher than the ratio 0.8 expected from laboratory measurements. The 9632 Å DIB is known to suffer from contamination by a photospheric Mg II line. However, unless there are other factors impacting this ratio in M17, the stellar contamination has to be, on average, higher

Table 3. DIB properties in the lines-of-sight to M17. The first column shows the rest wavelength of the DIBs. Columns 2 to 12 show the FWHM (nm; first row) and EW (mÅ; second row) measured for the sight lines towards the objects in M17.

λ	B111	B164	B215	B243	B253	B268	B275	B289	B311	B331	B337
4430	1.94 2027 \pm 32	2.1 2539 \pm 145	2.93 4794 \pm 218	1.69 1779 \pm 240	2.02 2020 \pm 158	1.89 1742 \pm 130	1.8 1919 \pm 36	2.33 3304 \pm 311	2.31 2528 \pm 53	– –	– –
5780	0.23 558 \pm 12	0.22 521 \pm 38	0.24 772 \pm 34	0.23 540 \pm 45	0.21 507 \pm 38	0.27 663 \pm 49	0.25 558 \pm 17	0.24 711 \pm 49	0.23 596 \pm 24	– –	– –
5797	0.11 89 \pm 8	0.14 129 \pm 32	– –	– –	– –	0.26 185 \pm 30	0.17 125 \pm 8	– –	0.15 168 \pm 8	– –	– –
6196	0.09 60 \pm 6	0.08 62 \pm 12	0.07 60 \pm 11	0.08 58 \pm 13	0.09 51 \pm 13	0.06 55 \pm 13	0.1 64 \pm 8	– –	0.09 63 \pm 6	– –	– –
6284	0.35 1691 \pm 11	0.29 1790 \pm 24	0.42 2206 \pm 28	0.25 1720 \pm 34	0.26 1708 \pm 38	0.33 1580 \pm 29	0.27 1661 \pm 36	0.35 1920 \pm 57	0.28 1770 \pm 25	– –	– –
6379	0.1 35 \pm 12	0.09 51 \pm 10	0.13 80 \pm 15	0.2 54 \pm 24	0.08 35 \pm 13	0.07 32 \pm 8	0.08 47 \pm 5	0.08 65 \pm 10	0.09 64 \pm 12	– –	– –
6614	0.14 188 \pm 6	0.14 203 \pm 27	0.13 251 \pm 12	0.13 187 \pm 19	0.13 168 \pm 15	0.14 201 \pm 20	0.14 203 \pm 27	0.14 243 \pm 29	0.13 227 \pm 11	– –	– –
7224	0.16 313 \pm 10	0.15 287 \pm 12	0.18 415 \pm 11	0.17 386 \pm 9	0.15 305 \pm 16	0.17 339 \pm 12	0.18 298 \pm 10	0.15 337 \pm 15	0.17 376 \pm 11	0.16 387 \pm 28	0.14 373 \pm 233
8620	– –	0.53 562 \pm 17	0.48 471 \pm 14	0.47 485 \pm 14	0.42 370 \pm 12	0.49 493 \pm 12	0.44 400 \pm 12	0.43 457 \pm 19	0.55 506 \pm 5	0.48 494 \pm 16	0.54 630 \pm 20
9577	0.44 371 \pm 14	0.45 579 \pm 11	0.48 546 \pm 22	0.47 479 \pm 13	0.55 512 \pm 20	0.45 435 \pm 11	0.42 439 \pm 10	0.45 526 \pm 13	0.45 632 \pm 17	0.4 328 \pm 23	0.47 489 \pm 16
9632	0.38 401 \pm 33	0.39 586 \pm 26	0.46 636 \pm 42	0.42 499 \pm 34	0.39 509 \pm 47	0.46 531 \pm 25	0.4 513 \pm 27	0.38 550 \pm 24	0.36 649 \pm 27	0.29 436 \pm 31	0.52 613 \pm 39
11797	0.32 278 \pm 13	0.27 262 \pm 14	0.32 205 \pm 15	0.39 306 \pm 33	0.31 269 \pm 29	0.36 336 \pm 18	0.21 173 \pm 44	0.27 255 \pm 20	0.26 261 \pm 14	0.64 318 \pm 31	0.99 457 \pm 49
13176	0.55 923 \pm 82	0.62 1134 \pm 47	0.67 1161 \pm 56	0.67 1115 \pm 108	0.62 1044 \pm 84	0.64 1016 \pm 76	0.35 463 \pm 70	0.54 928 \pm 71	0.53 859 \pm 53	0.53 796 \pm 60	0.73 1635 \pm 88
15268	0.46 395 \pm 34	0.71 875 \pm 25	0.58 521 \pm 42	– –	0.74 615 \pm 47	0.57 820 \pm 42	– –	0.52 438 \pm 18	0.51 401 \pm 17	– –	– –

than 150 mÅ in order to reduce the observed ratio to 0.8. This appears to require a rather large contribution from photospheric Mg II and we note that we cannot exclude systematic errors originating from telluric residuals.

In the optically thin limit the EW of the 9577 Å DIB can be converted into a column density. We do not use the 9632 Å DIB as it is known to suffer from photospheric line contamination which is difficult to correct for. For the observed 9577 Å DIB strengths this gives $N(\text{C}_{60}^+) = 2.5\text{--}4.3 \times 10^{13} \text{ cm}^{-2}$. These are somewhat lower abundances than the neutral C_{60} abundance of $2.4 \times 10^{14} \text{ cm}^{-2}/G_0$, where G_0 is the radiation field, measured with *Spitzer* in the diffuse ISM (Berné et al. 2017). However, the higher sensitivity of JWST opens the possibility to detect fullerene infrared emission (potentially both C_{60} and C_{60}^+ features) towards M17 that would allow a comparison between emission and absorption measurements in the same environment.

4.4. DIB profiles

Dahlstrom et al. (2013) reported on anomalous DIB profiles in the sight line towards Herschel 36. According to the authors, the profiles of the 5780, 5797, 6196, and 6614 DIBs show an extended red wing in comparison to nominal sight lines. Oka et al. (2013) confirmed this finding for three of the DIBs, but did not detect a pronounced red wing in the DIB at 6196 Å (we also do not detect a red wing in the profile of the 6196 DIB with the lower-resolution X-shooter data). These authors performed a study that allowed them to make a distinction between the carriers of the above DIBs at 5780, 5797, and 6614 DIBs and others (e.g. 5850, 6196, and 6379) which do not present such a pronounced red wing.

In addition, the sight line towards Herschel 36 shows absorption lines from rotationally excited CH^+ and CH and from vibrationally excited H_2 . Furthermore, an atypical extinction curve is observed with $R_V \sim 6$ and a weak 2175 Å bump, i.e., a flat far-UV extinction curve (Dahlstrom et al. 2013). M17 also shows

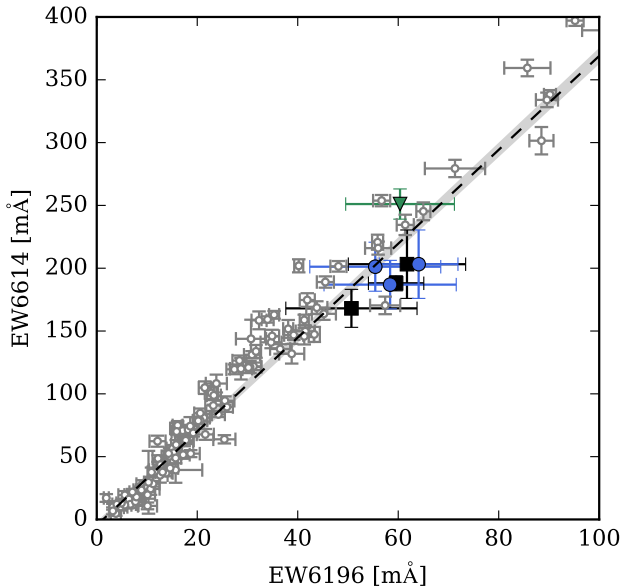


Fig. 4. Correlation between the DIBs at 6614 and 6196 Å. The dashed line represents the relation found by [McCall et al. \(2010\)](#) (grey dots) and the grey area shows the 1σ errors to the fit. The blue circles represent the sight lines towards objects with circumstellar disks, the green triangles towards stars with IR excess longwards of $2.5 \mu\text{m}$, and the black squares towards OB stars.

anomalous extinction ($R_V > 3.1$, [Paper I](#)), therefore, it is a good candidate to search for anomalous behaviour in the DIBs.

We compare the profiles of the DIBs towards M17 with the ones observed in the direction of Herschel 36 and HD 161061 (a nominal sight line) in [Fig. 5](#). The X-shooter spectra of Herschel 36 (unpublished) and the nominal sight line (HD 161061) were obtained previously by us with ESO programs 091.C-0934(B) and 385.C-0720(A). The spectra for these two sources were reduced using the same procedure described in [Sect. 2](#).

To facilitate the comparison, we have scaled the flux of the DIBs towards Herschel 36 and HD 161061 to match the depths of the cores of the DIBs towards M17. The profiles of the DIBs towards M17 are similar to the ‘nominal’ profile, and they do not show a red wing like in the case of Herschel 36. In the case of the 6196 Å DIB we do not detect a red wing in the spectrum of Herschel 36.

5. Comparison with other sight lines

For reddened lines of sight the strength of many DIBs increases in a roughly linear way with $E(B - V)$. The relation between the DIB strength and the reddening is not very well constrained for large extinction values because of the lack of data covering those high values of $E(B - V)$. Also, these studies have been applied to only a few prominent DIBs, mostly the 5797, 5780 and 6614 Å DIBs.

In [Fig. 6](#) we compare the behaviour of some prominent DIBs in M17 as a function of the reddening $E(B - V)$ with that in other published studies. We plot a linear fit to a large variety of Galactic sightlines ([Chlewicki et al. 1986](#); [Benvenuti & Porceddu 1989](#); [Herbig 1993](#); [Sonnenstrucker et al. 1997](#); [Krelowski et al. 1999](#); [Tuairisg et al. 2000](#); [Rawlings et al. 2003](#); [Galazutdinov et al. 2004](#); [Cox et al. 2005](#); [Friedman et al. 2011](#), for details see figure captions) excluding the star forming regions (M17, Herschel 36,

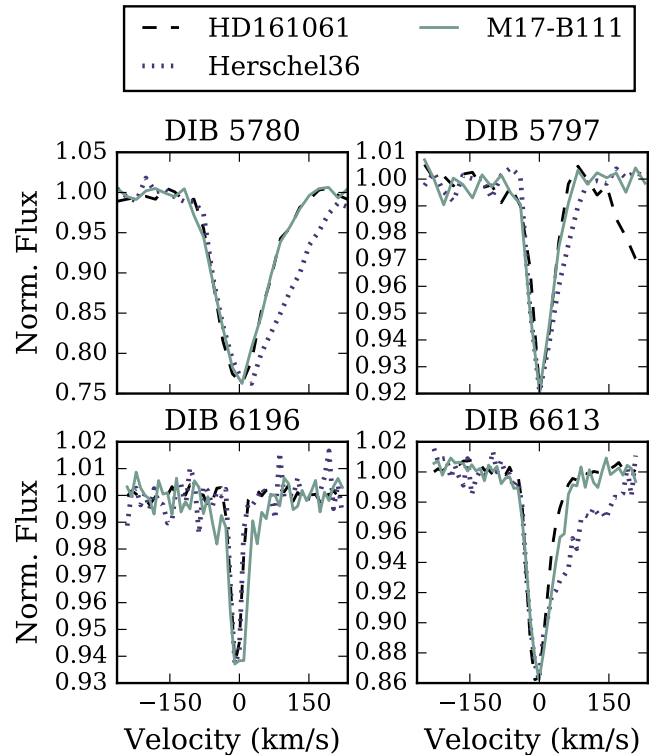


Fig. 5. Comparison of the shape of some DIBs towards M17 (B111, green, solid) with the sight line towards Herschel 36 (purple, dotted) and a ‘nominal’ sight line (black, dashed). All the spectra have been convolved to the same resolution and scaled to have the same line central depth. The M17 DIB profiles do not show an extended red wing, nor another anomaly with respect to the DIB in HD161061.

and RCW 36) for the three DIBs mentioned above with dashed black lines. With the grey area we show the linear fit and the 1σ error bars to the fit. For reference, we also plot DIB equivalent width measurements for Herschel 36 and for the massive star-forming region RCW 36 ([Ellerbroek et al. 2013](#)). The large scatter on these relations is intrinsic due to physical variations between lines-of-sight, and not due to measurement uncertainties. For example, [Vos et al. 2011](#) show that there is a dichotomy in the DIB strength versus extinction relation for UV exposed and UV shielded environments.

The M17 points are located below the average Galactic trend, like the sightlines probing the dense Cyg OB2 region. On the other hand, when including the DIBs towards M17 in the fit, the slope of the relation does not change significantly for each of the three DIBs.

We also compared the strength of the NIR DIB at 15268 Å as a function of $E(B - V)$ with several Galactic sight lines taken from the SDSS-III APOGEE survey by [Zasowski & Ménard \(2014\)](#). We do not show this comparison, but we observe that the sight lines towards M17 follow the same trend as the ones observed in different Galactic environments. We conclude that the DIB behaviour with respect to reddening $E(B - V)$, as observed in the direction of M17, indicates that these sightlines probe a denser ISM, but are not peculiar.

5.1. Ratio $EW(5797)/EW(5780)$

[Vos et al. \(2011\)](#) demonstrated that the ratio 5797/5780 might be useful to distinguish between sight lines probing diffuse cloud

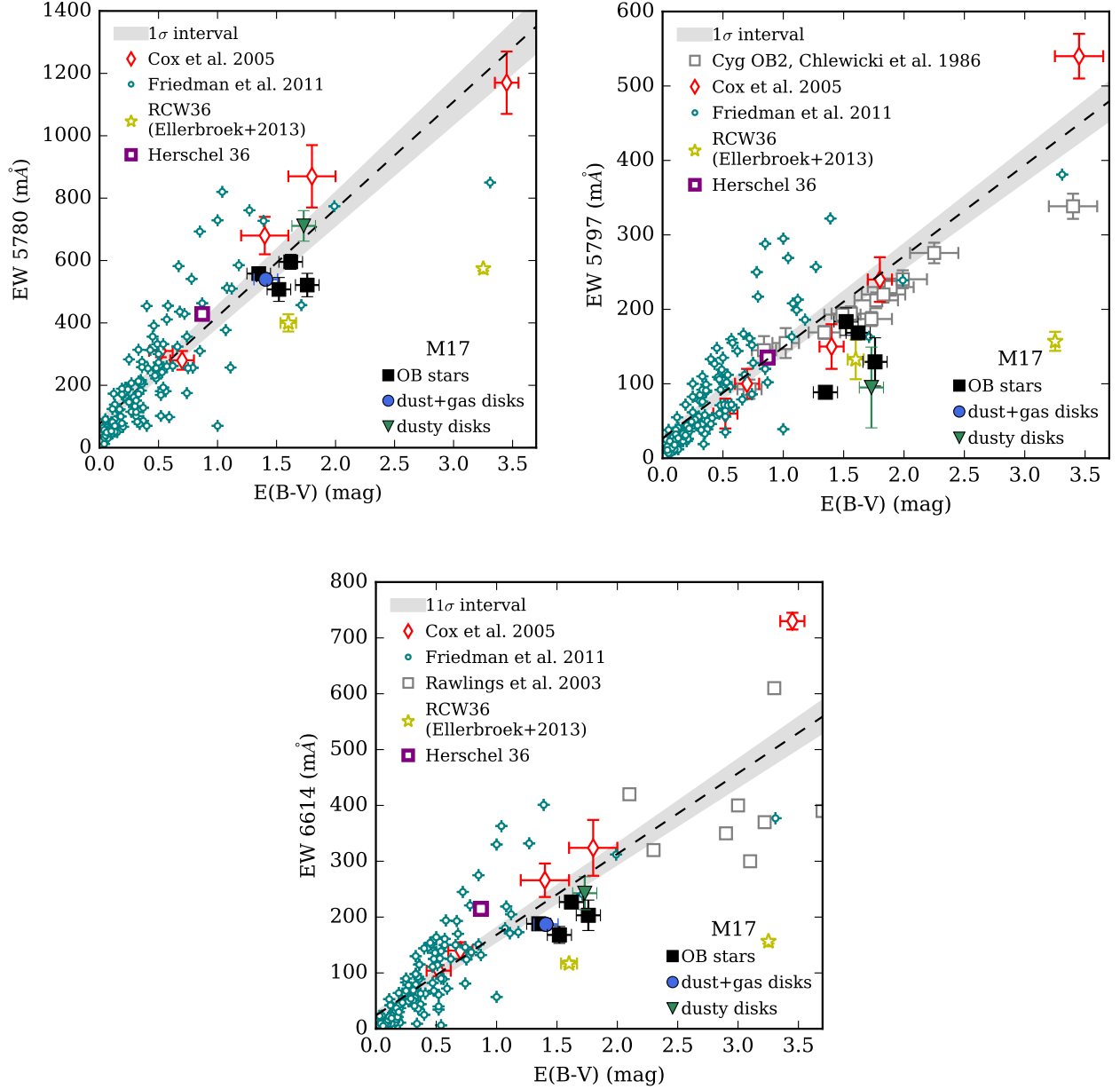


Fig. 6. Equivalent width of the 5780 (top left), 5797 (top right), and 6614 Å (bottom) DIBs as a function of reddening $E(B - V)$ for Galactic sightlines. The DIB strengths are taken from the literature (open symbols) and this work (filled symbols). The dashed line indicates the linear fit for the Galactic sight lines excluding the star forming regions (RCW 36, Herschel 36, and M17) and the grey area represents the 1σ error on the fit.

edges and denser cloud cores. The 5797 Å DIB is less sensitive to UV radiation than the 5780 Å DIB, therefore, one would expect that the 5797/5780 ratio is lower in higher extinction environments. This effect is strongest in sightlines dominated by one velocity component in the interstellar gas absorption profile (i.e. single-cloud sightlines) and tends to get 'washed-out' in multi-cloud sightlines. The EW ratio of the 5797/5780 DIBs is plotted in Fig. 7. Compared to the lower extinction data ($E(B-V) < 1$ mag; Friedman et al. 2011; Vos et al. 2011) the DIBs towards M17 cover a smaller range (0.15-0.45) in the 5797/5780 DIB ratio (though at higher extinction values). We do not find a clear correlation with spatial location in the cloud. Note that the interstellar gas absorption features of Ca II and Na I are largely unresolved at the spectral resolution of X-shooter. It is conceivable

that at higher spectral resolution the interstellar gas component associated with M17 will be resolved in multiple velocity components. This could imply that due to averaging along the line-of-sight the observed 5797/5780 ratio constitutes an average of this ratio in individual clouds. Variations of 5797/5780 (in diffuse ISM) are thought to depend strongly on the local geometry and the effective UV radiation field (see above), both of which are complex within the large H II region. Additionally, variations of the 5797/5780 ratio in the densest regions (high R_V) can potentially be driven by different mechanisms (e.g. depletion) as compared to changes in this ratio in the more diffuse medium (e.g. effective UV radiation field); this could be the case for M17 as the change on strength (per A_V) of these two DIBs with R_V is

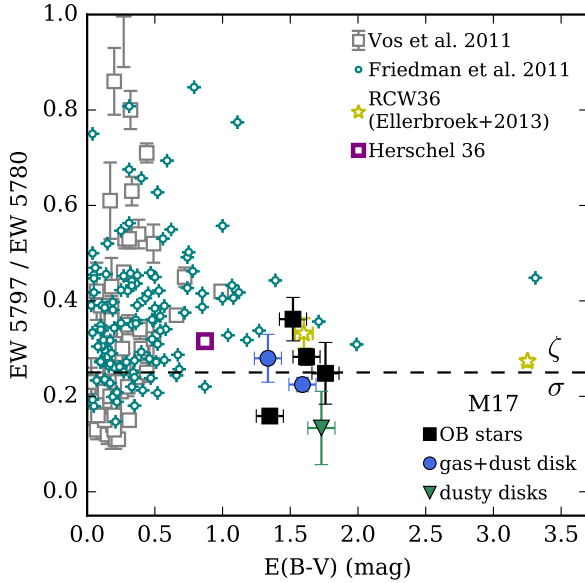


Fig. 7. The ratio of the 5797/5780 DIBs. The open symbols show data from the literature and the filled symbols data from the sightlines towards M17. The dashed line represents the division between ζ and σ type clouds.

different from each other as shown in Fig. 10 and discussed in Sect. 6.

5.2. 8620 DIB

The DIB at 8620 Å has recently gained more attention because it has been included in the large-scale surveys of RAVE and *Gaia*. It has been shown that the EW of this DIB is well correlated with the colour excess $E(B - V)$; Munari et al. (2008) reported a relation between the DIB strength and $E(B - V)$ given by $E(B - V) = (2.72 \pm 0.03) \times \text{EW } 8620 \text{ Å}$ for $E(B - V) < 1.2$.

Maíz Apellániz et al. (2015) measured this DIB in two sightlines with high extinction towards O stars in the cluster Berkeley 90. The authors detect at least two clouds moving at different velocities towards these objects; one thinner cloud, associated with the material far away from the stellar cluster, and a thicker one, associated with the material local to the cluster. The latter cloud is thicker for one sight line, which allowed the authors to measure the properties of DIBs in σ ($R_V \sim 4.5$) and in ζ ($R_V \sim 3.1$) clouds (see Sec. 5.1 for details about σ and ζ clouds). They observed that the DIB at 8620 Å is highly depleted in dense clouds and, therefore, correlates poorly with extinction higher than $A_V \sim 6$.

Damineli et al. (2016) extended the correlation of the 8620 DIB with extinction by adding sight lines with higher values of A_K . They used the extinction in the K band because it is less sensitive to the grain size than A_V . They adopted $A_{K_s} = 0.29E(B - V)$, which allowed to express the Munari et al. (2008) relation as $A_{K_s} = (0.691) \times \text{EW } 8620 \text{ Å}$. They find the correlation:

$$A_{K_s} = (0.612 \pm 0.013) \text{EW} + (0.191 \pm 0.025) \text{EW}^2. \quad (2)$$

This is in good agreement with Munari et al. (2008) for $\text{EW} < 0.6 \text{ Å}$ which translates to $A_V < 9 \text{ mag}$ for the extinction properties of their sample.

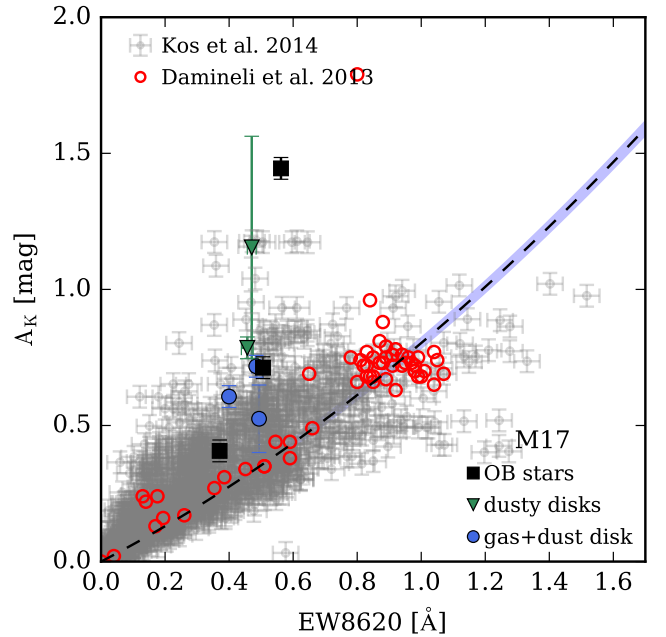


Fig. 8. K -band extinction A_K versus strength of the DIB at 8620 Å. The open symbols show data from the literature and the filled ones sightlines towards M17. The dotted line and the blue area show the relation in Eq. 2.

Using data from the RAVE survey, Kos et al. (2014) measured the strength of the 8620 Å DIB for $\sim 500\,000$ spectra at distances $< 3 \text{ kpc}$. We plot the EW of the 8620 Å DIB in Fig. 8. We include the data by Damineli et al. (2016, red dots) and Kos et al. (2014, grey dots), the black-dashed line and the blue shadow represent the relation in Eq. 2. In order to derive A_K from the Kos et al. (2014) data, we adopted $A_K/A_V = 0.11$.

The DIB strength towards M17 shows a very large spread in comparison with the relation by Damineli et al. (2016). This spread is similar to that observed in the sight lines from the RAVE survey. The large scatter in the M17 data could be an indication that the DIB carrier gets depleted at extinctions $A_K > 1.0$. We detect a general positive correlation between the strength of the 8620 DIB and the K -band extinction for $A_K \lesssim 1.0$.

6. DIB strengths versus R_V

The value of R_V is related to the size distribution of the dust grains. Large values of R_V imply a relative over-abundance of large grains, whereas small R_V values indicate that the small dust grains are more dominant in the size distribution. Typically higher values of R_V are associated with denser clouds where grain growth is or has been more significant than in diffuse regions. This is reflected in the relative slope of the extinction curve. Larger R_V values correspond to a flatter extinction curve, meaning that photons at all wavelengths get more equally absorbed.

Cardelli et al. (1989) presented observational evidence that the 2175 Å feature, normalised by the amount of extinction, shows a positive trend with R_V^{-1} . In Fig. 9 we present a similar plot, based on measurements recently collected by Xiang et al. (2017). Although the plot reveals significant scatter, there appears to be a general trend that sight lines with a smaller value of R_V show a stronger 2175 Å feature per magnitude visual extinction. The Pearson correlation coefficient between

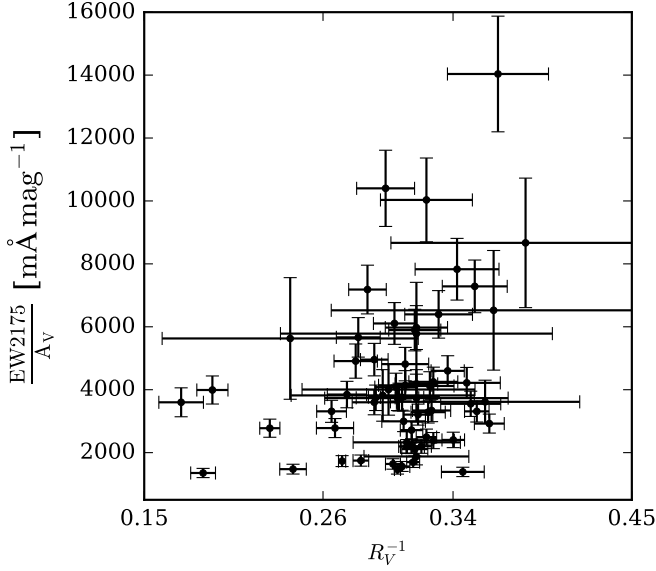


Fig. 9. Normalised EW of the 2175 Å feature measured in Galactic sight lines as a function of R_V . The measurements are obtained from Xiang et al. (2017). The 2175 Å feature is stronger in sight lines characterised by a smaller value of R_V .

EW(2175Å) and R_V^{-1} has a value of $r = 0.3$, which indicates a rather weak formal correlation.

In Fig. 10 we plot the strength of the DIBs normalised by the visual extinction A_V with R_V^{-1} . We include the sight lines towards M17, Herschel 36, and the object 408 in RCW 36. Where available, we add the data from Xiang et al. (2017) who compiled the EW of several DIBs in 97 sight lines. For most DIBs we discern a positive trend of the normalised DIB strength (EW/A_V) with R_V^{-1} , similar to the trend seen for the 2175 Å feature (Fig. 9). Given that A_V is in the denominator of both axes, if the uncertainties in A_V are large, a spurious relation between EW/A_V and R_V^{-1} might result. This is because when dividing by a very uncertain A_V , one could expect some values of both EW/A_V and R_V^{-1} to be very low and some to be very large causing a spurious linear relation intercepting at zero. However, we consider the errors in A_V are small enough – primarily due to the accurate spectral type determination – that we do not expect such an effect here.

We note that there is a cloud of data points centred at the Galactic average value of $R_V = 3.1$. The observed scatter could represent sampling of non-heterogeneous (multiple) interstellar cloud conditions in these sightlines. In other words, variations in DIB band strength (per unit reddening) are more pronounced than variations in *average* dust grain size. The presence of this cloud of data points shows that normalizing by A_V does not introduce a spurious relation. If that would be the case, we would expect the points at all R_V values to follow a linear relation. On the other hand, for sightlines with $R_V \gtrsim 3.8$ ($R_V^{-1} \lesssim 0.26$) there appears to be a much more pronounced (linear) relation between EW/A_V and R_V^{-1} . The M17 data presented here strengthen the presence of this linear relation that can already be gleaned from the data compiled by Xiang et al. (2017) where most of the sightlines with $R_V \gtrsim 3.8$ correspond to stars in star forming regions (Orion giant molecular cloud, Upper Scorpius, Trifid nebula, and Rho Ophiuchi).

Table 4. Results of the linear fit of EW/A_V versus R_V^{-1} towards M17 sightlines.

DIB	slope [mÅ/mag]	interception [mÅ/mag]	Pearson r
4430	1604 ± 403	-38 ± 97	0.39
5780	868 ± 195	-115 ± 45	0.80
5797	375 ± 110	-67 ± 26	0.63
6196	62 ± 24	-5 ± 5	0.91
6284	1705 ± 324	-137 ± 76	0.85
6379	17 ± 13	3 ± 3	0.21
6614	211 ± 56	-18 ± 13	0.88
7224	499 ± 99	-67 ± 23	0.70
8620	594 ± 130	-68 ± 30	0.69
11797	500 ± 106	-75 ± 24	0.46
13176	1714 ± 462	-254 ± 107	0.11
15268	1992 ± 551	-372 ± 128	0.63
9577	501 ± 107	-41 ± 25	0.62
9632	573 ± 121	-53 ± 28	0.82

We performed an orthogonal distance regression (ODR, Churchwell 1990)⁵ to fit a linear function to the DIB strength normalised by the visual extinction A_V versus R_V^{-1} for sightlines towards M17. The fit results, together with the Pearson correlation coefficients are listed in Table 4 and shown in Fig. 10 where the black line corresponds to the best fit to the M17 data alone and the shaded region to the 1σ error on the fit.

Based on the results from the fit, we confirm that for M17 there is a linear relation between the normalised DIB strength and R_V^{-1} . This correlation is strongest for the DIBs at 5780, 6196, 6284, 6614, and 9632 Å. From the Pearson correlation coefficient, r , we find that the correlation is moderate to strong ($r > 0.6$) for all DIBs except for those at 4430, 6379, 11797, and 13176 Å where the correlation is weak ($r < 0.5$). We note that for the 11797 and 13176 Å DIBs there is a clear outlier data point which strongly affects the Pearson correlation coefficient r (Fig. 10). This point corresponds to the B275 sight line where the spectral quality in the ranges of these two DIBs is poor, which could introduce systematic errors in the DIB measurements (see Figs. A.12 and A.13). Excluding this point results in $r > 0.7$ for both DIBs.

7. Discussion and conclusion

7.1. Extinction in M17

We calculated the extinction properties of the sight lines towards M17, with overall relatively large R_V values, using different methods; *i*) by dereddening the SED of the stars using Cardelli's extinction law and then fitting it to Kurucz models to find A_V and R_V (from that $E(B - V) = A_V/R_V$). *ii*) Directly by comparing the intrinsic magnitudes to the observed ones, to find A_V and $E(B - V)$ ($R_V = A_V/E(B - V)$). And *iii*) by finding A_V and $E(B - V)$ from the intrinsic and observed magnitudes and calculating R_V as defined by Fitzpatrick & Massa (2007, Eq. 1). We observe that the colour excess $E(B - V)$ calculated with Cardelli's extinction law and the SED fitting is systematically higher than using the other two methods. This confirms that this extinction law is not well suited for large values of R_V as already stated in Cardelli et al. (1989). We conclude that the best way of obtaining the extinction properties is to use the intrinsic and observed

⁵ Information about the python package is available at <https://docs.scipy.org/doc/scipy/reference/odr.html>

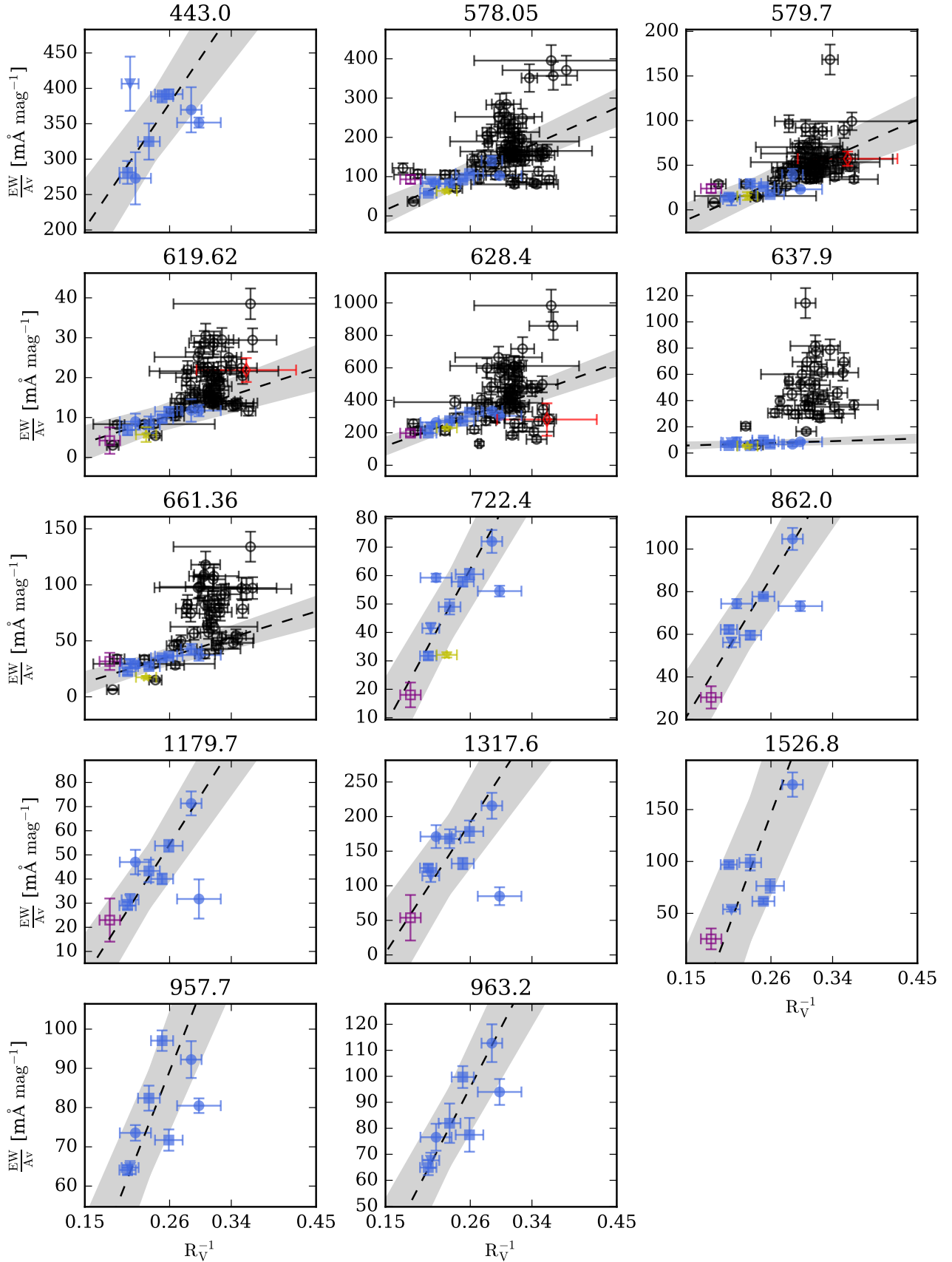


Fig. 10. Normalised DIB EW versus R_V^{-1} . The blue symbols show the M17 data; the dots show the stars in M17 with circumstellar disks, the triangles the stars with an IR excess longwards of $3\ \mu\text{m}$, and the squares the OB stars in M17. The open symbols show data from the literature. The purple square shows the position of Herschel 36, the yellow star shows the source 408 in RCW 36, and the red diamond shows the high mass X-ray binary 4U1907+09. The grey dots show the data by Xiang et al. (2017) when available. The black line shows a linear fit with R_V^{-1} and the shaded region the $1\text{-}\sigma$ error box of the fit to the M17 measurements only.

magnitudes and then calculate R_V as shown in Eq. 1, because with this equation it is also possible to take into account the NIR part of the SED.

7.2. Relation of DIBs with $E(B-V)$

In Fig. 6 we show the relation of the DIBs at 5780 and 5797 Å with the colour excess $E(B-V)$ in M17 and compare it with other sight lines published in the literature. $E(B-V)$ for the sight lines in M17 is relatively high compared to other Galactic sight lines; nevertheless, the DIB strength seems to follow the same trend as observed in other reddened sight lines.

Ellerbroek et al. (2013) reported an anomalous behaviour of the DIB strength in sight lines towards the star forming region RCW 36. We do not find a similar deviation in the sight lines towards M17. The behaviour reported in RCW 36 could be due to the way in which the authors calculated A_V . They assumed a value of $R_V = 3.1$, dereddened the spectrum using Cardelli's extinction law, and then fitted it to Kurucz models. In this paper we show that the value of $E(B-V)$ can be overestimated by as much as 0.5 mag (Fig. 2) when using Cardelli's extinction law. Previous studies have shown that star-forming regions such as M17 and M8 (where Herschel 36 resides) often show high values of R_V (e.g. Cardelli et al. 1989; Hanson et al. 1997). Therefore the assumption that $R_V = 3.1$ for RCW 36 probably underestimates its true R_V .

7.3. Relation of DIBs with R_V

The observed trend of $EW(DIB)/A_V$ with R_V^{-1} for M17 and other sightlines with $R_V \gtrsim 3.8$ ($R_V^{-1} \lesssim 0.26$; cf. Figure 10) is reminiscent to what Cardelli et al. (1989) and Xiang et al. (2017) find for the 2175 Å bump, the carrier of which is thought to consist of some (unidentified) carbonaceous material; however, the trend of the bump is weaker than that observed for the DIBs.

The slope of the linear relation between EW/A_V and R_V^{-1} (valid for $R_V \gtrsim 3.8$) can be interpreted as a measure of the sensitivity to which variations in the abundance of DIB carriers (per unit visual extinction) are related to variations in the average grain size of interstellar dust. This slope can then be interpreted in the context of either the depletion of the DIB carrier as the dust grains coagulate and grow (see e.g. Jura 1980; Ormel et al. 2009, EW/A_V decreases while R_V increases) or the production of DIB carriers as the larger grains get destroyed by the increasingly effective UV radiation field (see e.g. Cecchi-Pestellini et al. 1995; Jones 2004, EW/A_V increases and R_V decreases).

Alternatively, in the hypothesis that some DIB carriers are ionized species, the strengths of DIBs are expected to increase with a stronger effective UV radiation field. If R_V could be regarded as a tracer of the effective UV radiation field, higher values correspond to a lower ionization fraction, hence lower EW/A_V . In this context the slope of EW/A_V versus R_V^{-1} would be directly related to the ionization potential of the carrier species.

With the current data we can not distinguish between these different scenarios. However, it is possible to identify groups or families of DIB carriers which behave similarly in the transition from the more dense to diffuse ISM (high to low R_V). To investigate this we compared the column density of the DIB carriers multiplied by the (unknown) oscillator strength, Nf , with the slope $d(EW/A_V)/dR_V^{-1}$ (cf. Fig. 10; Table 4). This slope can be viewed as a measure of the sensitivity of the DIB carriers to changes in R_V^{-1} , hence in grain size distribution or as a measure of the carrier's ionization potential. We will refer to this slope

as the DIB- R_V sensitivity. Assuming that the optically-thin approximation holds for the DIBs (no saturation of absorption) we have:

$$Nf = 1.13 \times 10^{20} \frac{EW}{\lambda^2} \quad (3)$$

where N is the column density in cm^{-2} , f the oscillator strength, EW is the equivalent width (in Å) and λ is the central wavelength of each DIB (in Å). We show the dependence of the DIB- R_V sensitivity on $Nf\lambda^2$, and Nf in Fig. 11; In both cases a linear fit is shown with a dashed line and the shaded region shows the 2σ error to the fit. Additionally we marked the C_{60}^+ DIBs with green pentagons.

First we discuss the results in the context of R_V as a proxy for changes in the grain size distribution.

We are able to identify two groups; the first group contains ten moderately strong DIBs, including the two C_{60}^+ DIBs, the DIBs presenting a red wing in Herschel 36 (5780, 5797, and 6614), and those at 6196, 6379, 7224, 8620, and 11797 Å. These DIBs show a modest sensitivity to the change in grain size, and their sensitivity increases about linearly as a function of DIB strength. The second group consists of four strong DIBs (at 4430, 6284, 13176, and 15268 Å), that are very sensitive to the change in grain size distribution (large $d(EW/A_V)/dR_V^{-1}$ slope values), but their DIB- R_V sensitivity does not seem to depend on the DIB strength.

In the case of the first group, we postulate that the observed linear increase of the DIB- R_V sensitivity with the amount of DIB carriers, Nf , suggests that the increase of the latter is primarily due to an increase in column density and that f is quite similar for this group of DIB carriers. This is because the reverse situation, i.e. that a systematic increase of the sensitivity of DIB carriers to changes in R_V is related to a systematic increase of the oscillator strength of the DIB carriers appears much more unlikely. If this is the case, the oscillator strengths of these DIBs could be extracted with reference to the two DIBs at 9577 and 9632 Å assigned to C_{60}^+ ($f_{9577} = 0.018$ and $f_{9632} = 0.015$).

The linear dependency of the DIB- R_V sensitivity on the DIB strength implies that the relative production/destruction rate of these DIB carriers is the same for the same change in typical grain size (R_V). In other words, for a doubling of the abundance of DIB carriers in the first group, the same change in grain size distribution is required. This may imply a common production/destruction mechanism. The fact that the DIB- R_V sensitivity of the stronger DIBs is independent of their strength suggests the existence of an additional reservoir of DIB carriers unrelated to the dust grains. These carriers would be produced/destroyed as the grain size distribution changes as well as via other mechanisms.

Alternatively, we consider the scenario where R_V is a proxy of the effective UV radiation field strength and the DIB carriers are large ionised molecules. In this case Fig. 11 has to be interpreted differently. Here the slope $d(EW/A_V)/dR_V^{-1}$ is an indirect measure of the carrier's ionization potential. The broad DIBs at 15268, 13176, 6284 and 4430 Å have a (similar) strong slope which implies a (similar) low ionization potential. The ionization potential of the carriers of these broad DIBs is then expected to be significantly lower than the ionization potential of 7.58 eV measured for C_{60} (de Vries et al. 1992). In the opposite direction, the narrow DIBs at 7224, 5797, 6614, 6196, and 6379 Å which have increasingly shallower slopes should then have increasingly higher ionization potentials. For PAHs the ionisation potential is strongly related to their number of π -electrons (see Fig. B.1. in Ruiterkamp et al. 2005).

We note that in the case that there are several foreground clouds contributing to the extinction in the sightline towards M17, the interpretation of the observed relations is complicated. The hypotheses presented above assume that most of the variation in A_V and R_V arises from the dust and gas in the M17 region. Correcting for a foreground sheet of dust, with $A_V = 2$ and a constant foreground $\text{EW(DIB)}/A_V$ contribution projected across the M17 region, would shift all the EW/A_V values vertically. Also, correcting for foreground dust with a nominal $R_V = 3.1$, will slightly increase the R_V values derived for the local M17 dust, but have little impact on the slope of the relation between $\text{EW(DIB)}/A_V$ and R_V^{-1} . It could also affect the mean normalised line strengths. The above scenarios and hypotheses can be further tested by examining the relation between $\text{EW(DIB)}/A_V$ and R_V for other star forming regions that probe a range of extinction properties and grain size distributions, similar to M17. This will also help to disentangle the impact of foreground dust extinction and to determine possible effects due to measurement uncertainties.

8. Summary

We present an analysis of the properties of the DIBs in sight lines toward the star forming region M17 in comparison to the properties of nominal DIBs as well as DIBs that have been reported to be anomalous.

- Cardelli's extinction law is not suitable for large values of R_V . The best way of calculating the extinction parameters A_V and $E(B - V)$, when the spectral type of the observed star is known, is by directly comparing the observed and intrinsic magnitudes. By using the relation between R_V and $E(V - K)/E(B - V)$ of [Fitzpatrick & Massa \(2007\)](#) it is possible to calculate A_K and, therefore the K -band excess produced by the circumstellar disk.
- From the observed C_{60}^+ DIB at 9577 Å we derive a column density $N(C_{60}^+) = 2.5 - 4.3 \times 10^{13} \text{ cm}^{-2}$.
- We also detect the NIR DIBs at 11797, 13176, and 15268 Å in the sightlines towards M17.
- The profiles of the DIBs toward M17 do not present a red wing, in contrast to those towards Herschel 36. This indicates that the red wing is not common to star forming regions, but that the environment towards Herschel 36 must present some special properties that cause the DIBs to have a red wing.
- The strength of the 5780 Å DIBs towards M17 is as expected from the relations found in the literature for their values of $E(B - V)$. The 5797 Å DIBs show a relatively large spread in relation to other Galactic DIBs, and the 6614 Å DIBs towards M17 are slightly weaker than expected for their $E(B - V)$ values.
- In the M17 region we find trends between the strength of the studied DIBs (per unit visual extinction) and R_V^{-1} , most notably for the 6196 and 7224 Å DIBs. The trend remains when we include the sightlines towards star forming regions presented in [Xiang et al. \(2017\)](#). For sightlines with $R_V \sim 3.1$ there is no trend.
- The slope values of the linear relation between the DIBs EW normalised by A_V and R_V^{-1} (DIB- R_V sensitivity) allow us to identify two main groups of DIBs in terms of their sensitivity to R_V (for $R_V > 3.8$, $R_V^{-1} < 0.26$). The first group consists of DIBs with similar sensitivity to changes in R_V as the two C_{60}^+ DIBs: 5780, 5797, 7224, 8620, 9577, 9632, and 11797 Å. For this group we find that the DIB- R_V sensitivity varies linearly with DIB strength. The second group consists of DIBs with roughly three times stronger DIB- R_V sensitivity: 4430, 6284, 13176, and 15268 Å; for this group, the DIB- R_V sensitivity does not depend on the DIB strength. This response of DIB carriers to changes in interstellar dust properties provides additional clues to the (dis)similarity of different DIB carriers, and may provide clues as to their production/destruction mechanisms, and can thus ultimately help with their identifications.
- Three scenarios are proposed for the observed behaviour of DIBs in star-forming regions (with $R_V > 3.8$): (1) DIB carriers stick to dust grains, and thus get depleted from the gas phase, as the grains grow in size (dust-coagulation) in the denser regions of interstellar clouds; (2) DIB carriers are produced from the dust grains in the strong UV radiation fields in these regions which lead to increased abundances of DIB carriers (and that of the 2715 Å band) and, by direct consequence, a decrease of the average dust particle size. (3) As R_V decreases and the effective UV radiation field strength increases, the ionization fraction of the parent carriers increases thus causing the DIBs related to ionized molecular carriers to become stronger. The effective response of DIB strength to changes in the UV radiation field, i.e. $d(\text{EW}/A_V)/dR_V^{-1}$, is then a measure of the carriers ionization potential. At this point we can not distinguish between these scenarios. Further investigations of specific (star forming) regions that probe a range of R_V values, like M17, are needed to examine the relation between DIB strength and R_V .

Acknowledgements. Based on observations collected at the European Organisation for Astronomical Research in the Southern Hemisphere under ESO program(s) 091.C-0934(B) (Herschel 36), 385.C-0720(A) (HD161056) and 60.A-9404(A), 085.D-0741, 089.C-0874(A), 091.C-0934(B) (M17). The authors thank Rens Waters, Martin Heemskerk, Juan Hernandez Santisteban, Lucia Klarman, Samayra Straal, Marieke van Doesburgh, Xander Tielens, and Rosine Lallement for discussions that helped to improve this paper. This research made use of Astropy, a community-developed core Python package for Astronomy ([The Astropy Collaboration et al. 2018](#)), NASA's Astrophysics Data System Bibliographic Services (ADS), and the SIMBAD database, operated at CDS, Strasbourg, France ([Wenger et al. 2000](#)).

References

- Benvenuti, P. & Porceddu, I. 1989, *A&A*, 223, 329
 Berné, O., Cox, N. L. J., Mulas, G., & Joblin, C. 2017, *A&A*, 605, L1
 Broos, P. S., Feigelson, E. D., Townsley, L. K., et al. 2007, *ApJS*, 169, 353
 Cami, J. & Cox, N. L. J., eds. 2014, *IAU Symposium*, Vol. 297, *The Diffuse Interstellar Bands*
 Campbell, E. K., Holz, M., Gerlich, D., & Maier, J. P. 2015, *Nature*, 523, 322
 Capitano, L., Lallement, R., Vergely, J. L., Elyajouri, M., & Monreal-Ibero, A. 2017, *A&A*, 606, A65
 Cardelli, J. A., Clayton, G. C., & Mathis, J. S. 1989, *ApJ*, 345, 245
 Castelli, F. & Kurucz, R. L. 2004, *ArXiv Astrophysics e-prints* [astro-ph/0405087]
 Cecchi-Pestellini, C., Aiello, S., & Barsella, B. 1995, *ApJS*, 100, 187
 Chini, R., Elsaesser, H., & Neckel, T. 1980, *A&A*, 91, 186
 Chini, R. & Kruegel, E. 1983, *A&A*, 117, 289
 Chlewicki, G., van der Zwet, G. P., van Ijzendoorn, L. J., Greenberg, J. M., & Alvarez, P. P. 1986, *ApJ*, 305, 455
 Churchwell, E. 1990, in *Contemporary mathematics (American Mathematical Society)*, Vol. 112, *Hot Star Workshop III: The Earliest Phases of Massive Star Birth*, ed. P. Brown & W. Fuller, 186
 Cox, N. L. J., Cami, J., Kaper, L., et al. 2014, *A&A*, 569, A117
 Cox, N. L. J., Cordiner, M. A., Ehrenfreund, P., et al. 2007, *A&A*, 470, 941
 Cox, N. L. J., Kaper, L., Foing, B. H., & Ehrenfreund, P. 2005, *A&A*, 438, 187
 Cutri, R. M., Skrutskie, M. F., van Dyk, S., et al. 2003, *VizieR Online Data Catalog*, 2246
 Dahlstrom, J., York, D. G., Welty, D. E., et al. 2013, *ApJ*, 773, 41
 Damineli, A., Almeida, L. A., Blum, R. D., et al. 2016, *MNRAS*, 463, 2653

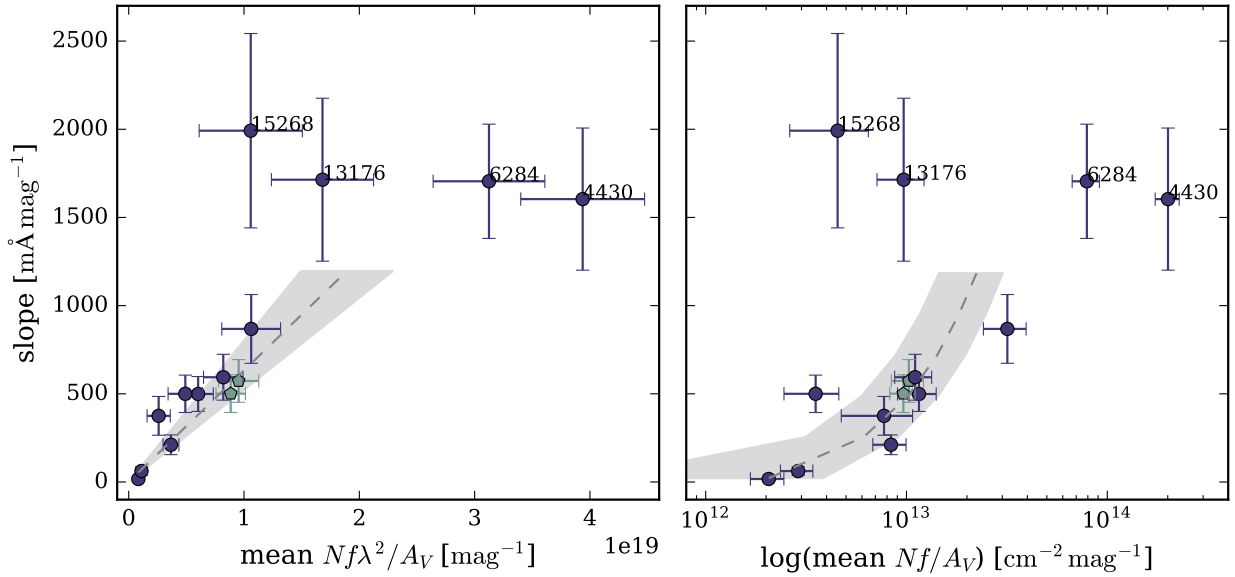


Fig. 11. Slope representing the sensitivity of EW/A_V with changes in R_V^{-1} versus mean A_V normalised line strength (left; expressed as Nf/A_V) and versus the log of this quantity (right) for all sightlines. The dashed line and the shaded regions represent the linear fit to the group of DIBs with slopes ≤ 1000 and the 2σ error bars to the fit. The two C^+_{60} DIBs are represented with light green pentagons.

de Vries, J., Steger, H., Kamke, B., et al. 1992, *Chemical Physics Letters*, 188, 159
 Drimmel, R., Cabrera-Lavers, A., & López-Corredoira, M. 2003, *A&A*, 409, 205
 Ehrenfreund, P., Cami, J., Jiménez-Vicente, J., et al. 2002, *ApJ*, 576, L117
 Ellerbroek, L. E., Podio, L., Kaper, L., et al. 2013, *A&A*, 551, A5
 Fitzpatrick, E. L. 1999, *PASP*, 111, 63
 Fitzpatrick, E. L. & Massa, D. 2007, *ApJ*, 663, 320
 Freudling, W., Romaniello, M., Bramich, D. M., et al. 2013, *A&A*, 559, A96
 Friedman, S. D., York, D. G., McCall, B. J., et al. 2011, *ApJ*, 727, 33
 Galazutdinov, G. A., Manicò, G., Pirronello, V., & Królowski, J. 2004, *MNRAS*, 355, 169
 Geballe, T. R., Najarro, F., Figer, D. F., Schlegelmilch, B. W., & de La Fuente, D. 2011, *Nature*, 479, 200
 Gordon, K. D. & Clayton, G. C. 1998, *ApJ*, 500, 816
 Gordon, K. D., Clayton, G. C., Misselt, K. A., Landolt, A. U., & Wolff, M. J. 2003, *ApJ*, 594, 279
 Hamano, S., Kobayashi, N., Kondo, S., et al. 2015, *ApJ*, 800, 137
 Hanson, M. M., Howarth, I. D., & Conti, P. S. 1997, *ApJ*, 489, 698
 Herbig, G. H. 1993, *ApJ*, 407, 142
 Hobbs, L. M., York, D. G., Thorburn, J. A., et al. 2009, *ApJ*, 705, 32
 Hoffmeister, V. H., Chini, R., Scheyda, C. M., et al. 2008, *ApJ*, 686, 310
 Joblin, C., D'Hendecourt, L., Leger, A., & Maillard, J. P. 1990, *Nature*, 346, 729
 Jones, A. P. 2004, in *Astronomical Society of the Pacific Conference Series*, Vol. 309, *Astrophysics of Dust*, ed. A. N. Witt, G. C. Clayton, & B. T. Draine, 347
 Jura, M. 1980, *ApJ*, 235, 63
 Kausch, W., Noll, S., Smette, A., et al. 2015, *A&A*, 576, A78
 Kos, J., Zwitter, T., Wyse, R., et al. 2014, *Science*, 345, 791
 Królowski, J., Ehrenfreund, P., Foing, B. H., et al. 1999, *A&A*, 347, 235
 Królowski, J., Galazutdinov, G. A., Bondar, A., & Beletsky, Y. 2016, *MNRAS*, 460, 2706
 Kurucz, R. L. 1993, *VizieR Online Data Catalog*, 6039
 Maíz Apellániz, J., Barbá, R. H., Sota, A., & Simón-Díaz, S. 2015, *A&A*, 583, A132
 Mathis, J. S., Rimpl, W., & Nordsieck, K. H. 1977, *ApJ*, 217, 425
 McCall, B. J., Drosback, M. M., Thorburn, J. A., et al. 2010, *ApJ*, 708, 1628
 Mennella, V., Colangeli, L., Bussoletti, E., Palumbo, P., & Rotundi, A. 1998, *ApJ*, 507, L177
 Mishra, A. & Li, A. 2015, *ApJ*, 809, 120
 Misselt, K. A., Clayton, G. C., & Gordon, K. D. 1999, *ApJ*, 515, 128
 Modigliani, A., Goldoni, P., Royer, F., et al. 2010, in *Proc. SPIE*, Vol. 7737, *Observatory Operations: Strategies, Processes, and Systems III*, 773728
 Munari, U., Tomasella, L., Fiorucci, M., et al. 2008, *A&A*, 488, 969
 Oka, T., Welty, D. E., Johnson, S., et al. 2013, *ApJ*, 773, 42
 Ormel, C. W., Paszun, D., Dominik, C., & Tielens, A. G. G. M. 2009, *A&A*, 502, 845
 Pecaut, M. J. & Mamajek, E. E. 2013, *ApJS*, 208, 9
 Povich, M. S., Churchwell, E., Bieging, J. H., et al. 2009, *ApJ*, 696, 1278
 Prisinzano, L., Damiani, F., Micela, G., & Pillitteri, I. 2007, *A&A*, 462, 123

Puls, J., Urbaneja, M. A., Venero, R., et al. 2005, *A&A*, 435, 669
 Ramírez-Tannus, M. C., Kaper, L., de Koter, A., et al. 2017, *A&A*, 604, A78
 Rawlings, M. G., Adamson, A. J., & Whittet, D. C. B. 2003, *MNRAS*, 341, 1121
 Reid, M. J., Menten, K. M., Zheng, X. W., et al. 2009, *ApJ*, 700, 137
 Rivero González, J. G., Puls, J., Najarro, F., & Brott, I. 2012, *A&A*, 537, A79
 Ruiterkamp, R., Cox, N. L. J., Spaans, M., et al. 2005, *A&A*, 432, 515
 Schulz, A., Lenzen, R., Schmidt, T., & Proetel, K. 1981, *A&A*, 95, 94
 Smette, A., Sana, H., Noll, S., et al. 2015, *A&A*, 576, A77
 Snow, T. P. 2014, in *IAU Symposium*, Vol. 297, *The Diffuse Interstellar Bands*, ed. J. Cami & N. L. J. Cox, 3–12
 Snow, T. P., Welty, D. E., Thorburn, J., et al. 2002, *ApJ*, 573, 670
 Sonnentrucker, P., Cami, J., Ehrenfreund, P., & Foing, B. H. 1997, *A&A*, 327, 1215
 The Astropy Collaboration, Price-Whelan, A. M., Sipőcz, B. M., et al. 2018, *ArXiv e-prints [arXiv:1801.02634]*
 Tuairisg, S. Ó., Cami, J., Foing, B. H., Sonnentrucker, P., & Ehrenfreund, P. 2000, *A&AS*, 142, 225
 Vernet, J., Dekker, H., D'Odorico, S., et al. 2011, *A&A*, 536, A105
 Vos, D. A. I., Cox, N. L. J., Kaper, L., Spaans, M., & Ehrenfreund, P. 2011, *A&A*, 533, A129
 Wegner, W. 2000, *MNRAS*, 319, 771
 Wegner, W. 2014, *Acta Astron.*, 64, 261
 Welty, D. E., Federman, S. R., Gredel, R., Thorburn, J. A., & Lambert, D. L. 2006, *ApJS*, 165, 138
 Wenger, M., Ochsenbein, F., Egret, D., et al. 2000, *A&AS*, 143, 9
 Xiang, F. Y., Li, A., & Zhong, J. X. 2011, *ApJ*, 733, 91
 Xiang, F. Y., Li, A., & Zhong, J. X. 2017, *ApJ*, 835, 107
 Xu, Y., Moscadelli, L., Reid, M. J., et al. 2011, *ApJ*, 733, 25
 Zasowski, G. & Ménard, B. 2014, in *IAU Symposium*, Vol. 297, *The Diffuse Interstellar Bands*, ed. J. Cami & N. L. J. Cox, 68–73

Appendix A: Observed DIBs and gaussian fits

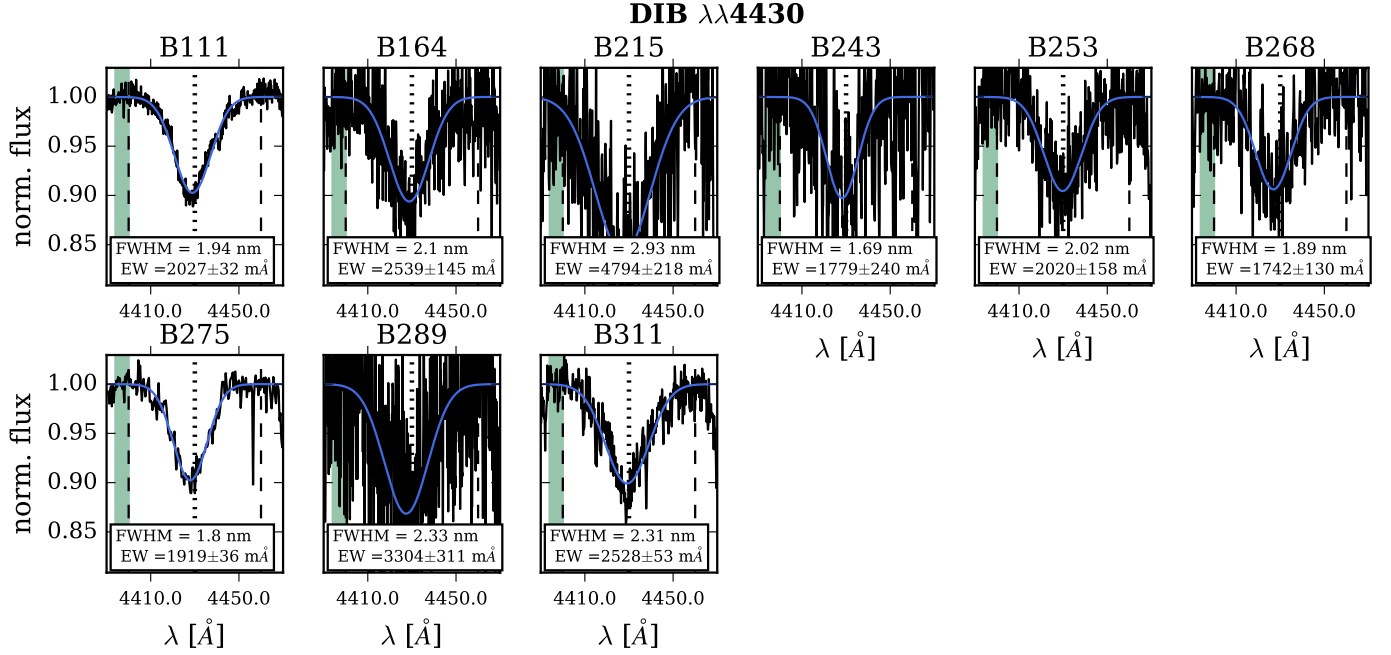


Fig. A.1. DIB profiles at 4430 Å. The vertical dashed lines show the integration limits used to calculate the DIB strength, the dotted line shows the central wavelength of the DIB, and the green shaded region shows the region in which the error was calculated. With a solid-blue line we show the Gaussian fit to the DIB profile. The white box in the bottom of each panel indicated the FWHM and EW of this DIB for each object.

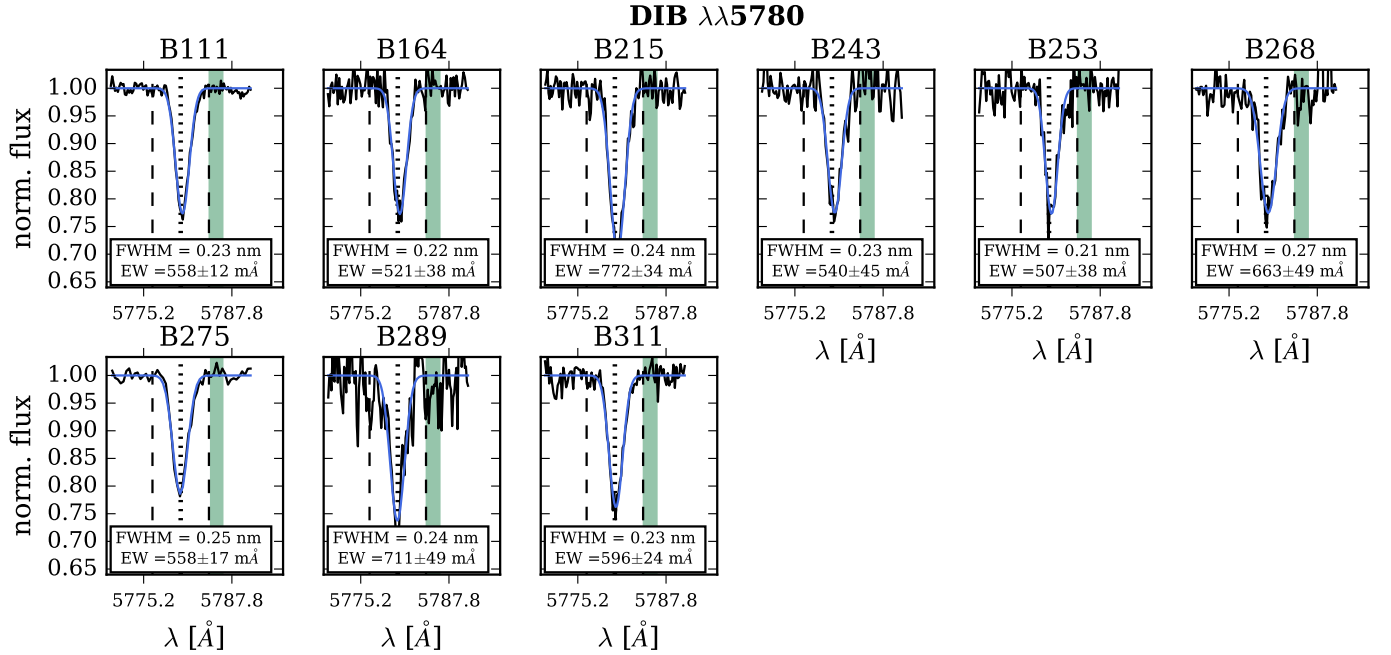


Fig. A.2. DIB profiles at 5780 Å. The vertical dashed lines show the integration limits used to calculate the DIB strength, the dotted line shows the central wavelength of the DIB, and the green shaded region shows the region in which the error was calculated. With a solid-blue line we show the Gaussian fit to the DIB profile. The white box in the bottom of each panel indicated the FWHM and EW of this DIB for each object.

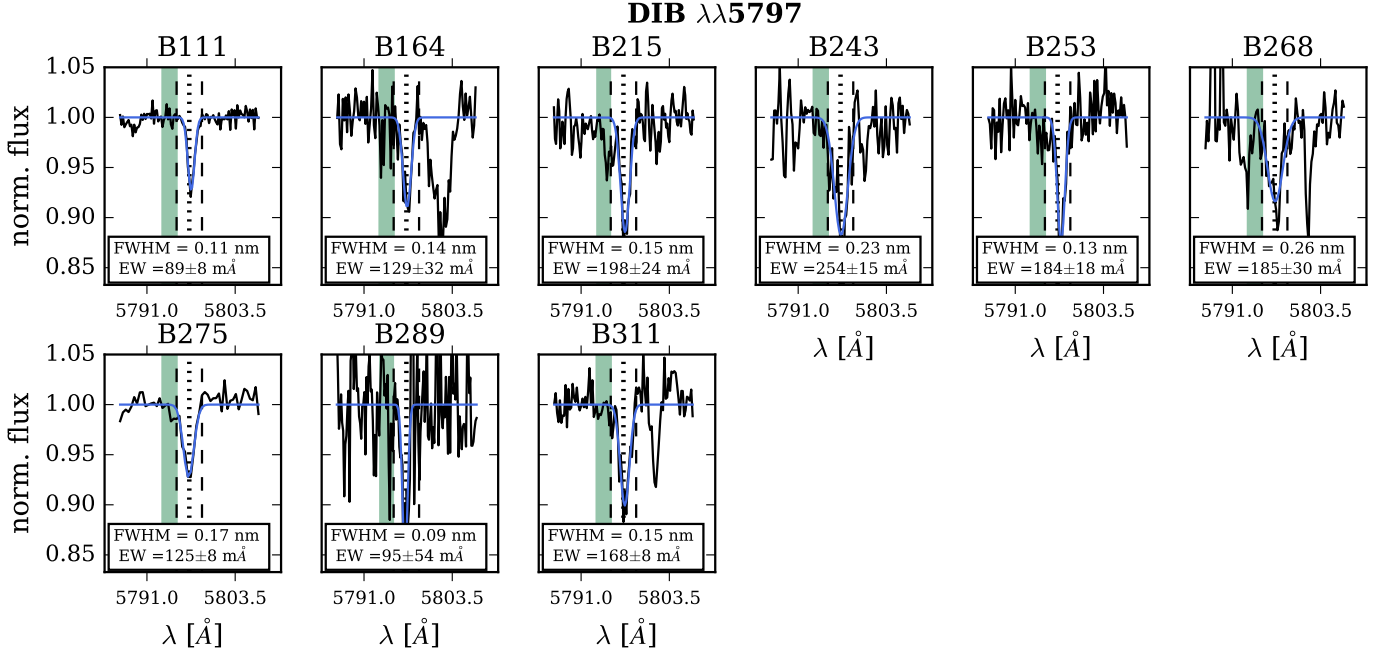


Fig. A.3. DIB profiles at 5798 Å. The vertical dashed lines show the integration limits used to calculate the DIB strength, the dotted line shows the central wavelength of the DIB, and the green shaded region shows the region in which the error was calculated. With a solid-blue line we show the Gaussian fit to the DIB profile. The white box in the bottom of each panel indicated the FWHM and EW of this DIB for each object.

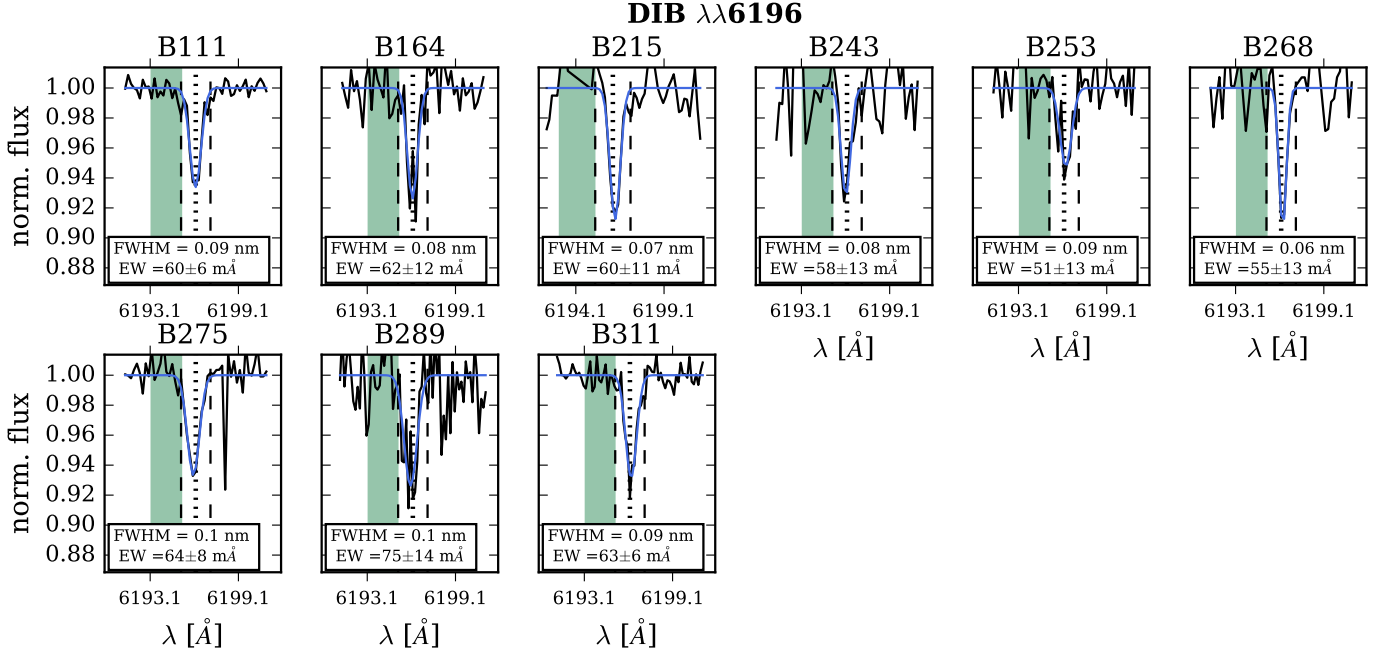


Fig. A.4. DIB profiles at 6196 Å. The vertical dashed lines show the integration limits used to calculate the DIB strength, the dotted line shows the central wavelength of the DIB, and the green shaded region shows the region in which the error was calculated. With a solid-blue line we show the Gaussian fit to the DIB profile. The white box in the bottom of each panel indicated the FWHM and EW of this DIB for each object.

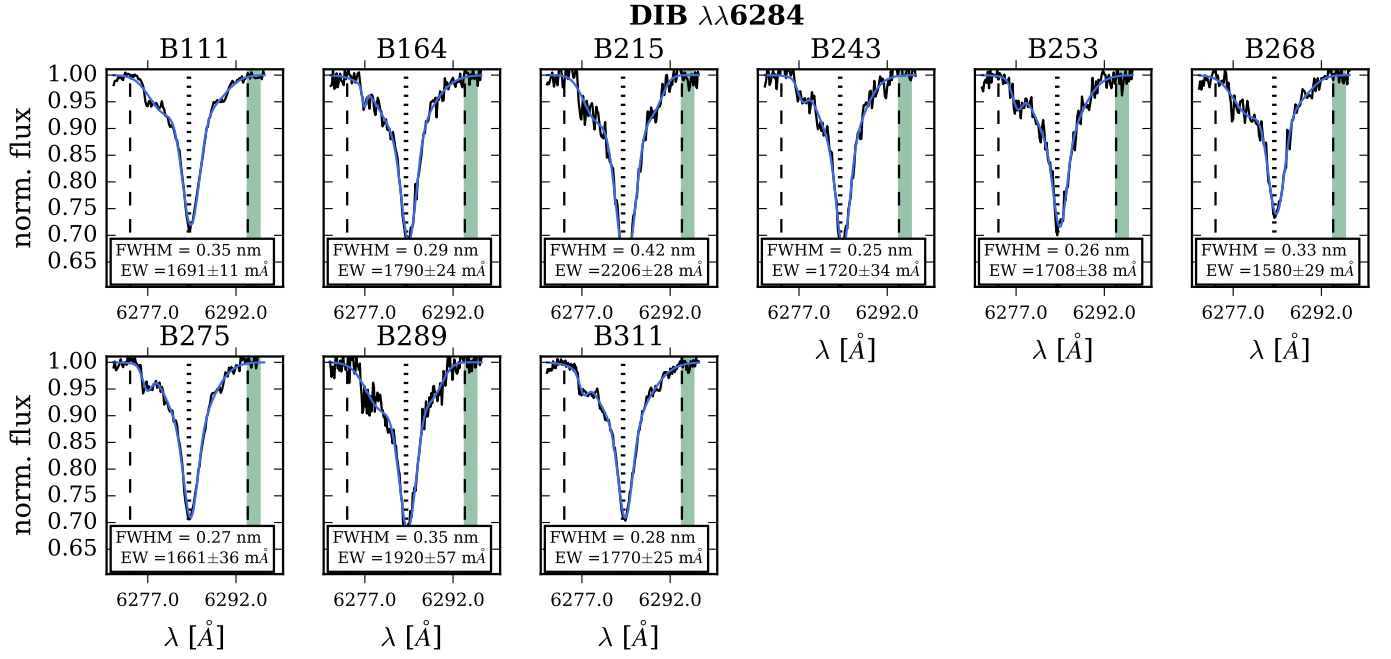


Fig. A.5. DIB profiles at 6284 Å. The vertical dashed lines show the integration limits used to calculate the DIB strength, the dotted line shows the central wavelength of the DIB, and the green shaded region shows the region in which the error was calculated. With a solid-blue line we show the Gaussian fit to the DIB profile. The white box in the bottom of each panel indicated the FWHM and EW of this DIB for each object.

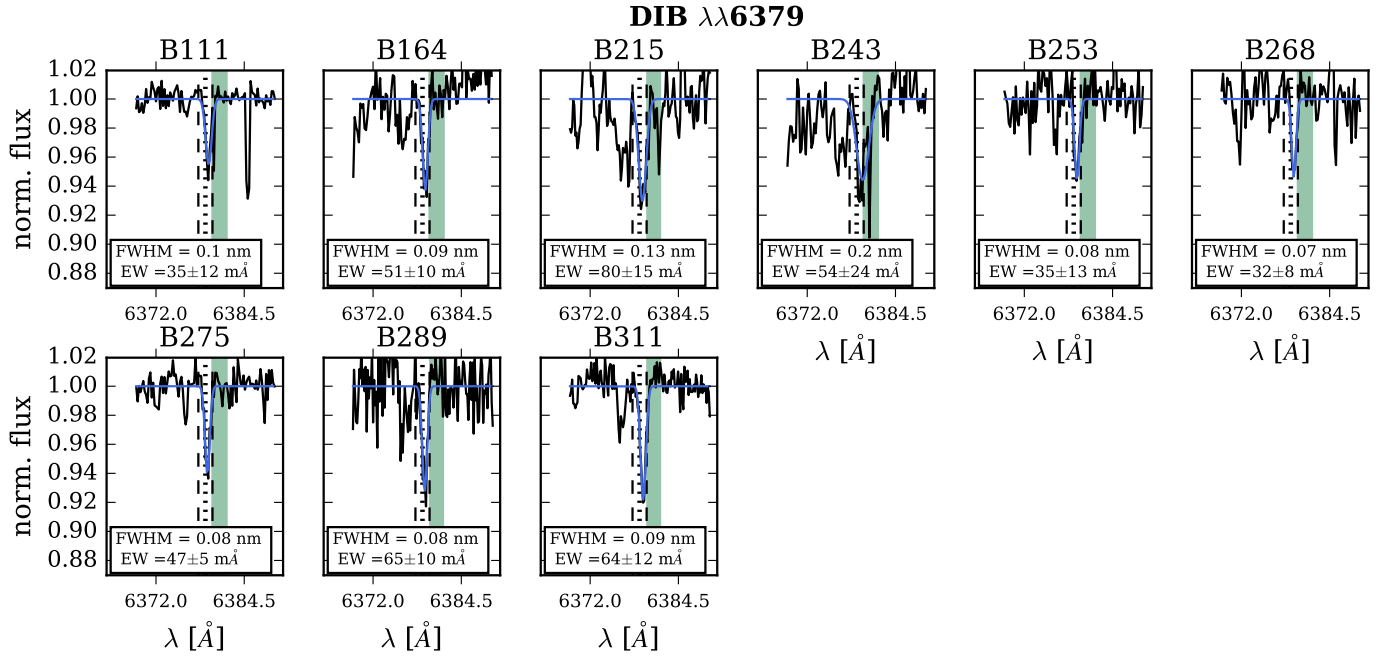


Fig. A.6. DIB profiles at 6379 Å. The vertical dashed lines show the integration limits used to calculate the DIB strength, the dotted line shows the central wavelength of the DIB, and the green shaded region shows the region in which the error was calculated. With a solid-blue line we show the Gaussian fit to the DIB profile. The white box in the bottom of each panel indicated the FWHM and EW of this DIB for each object.

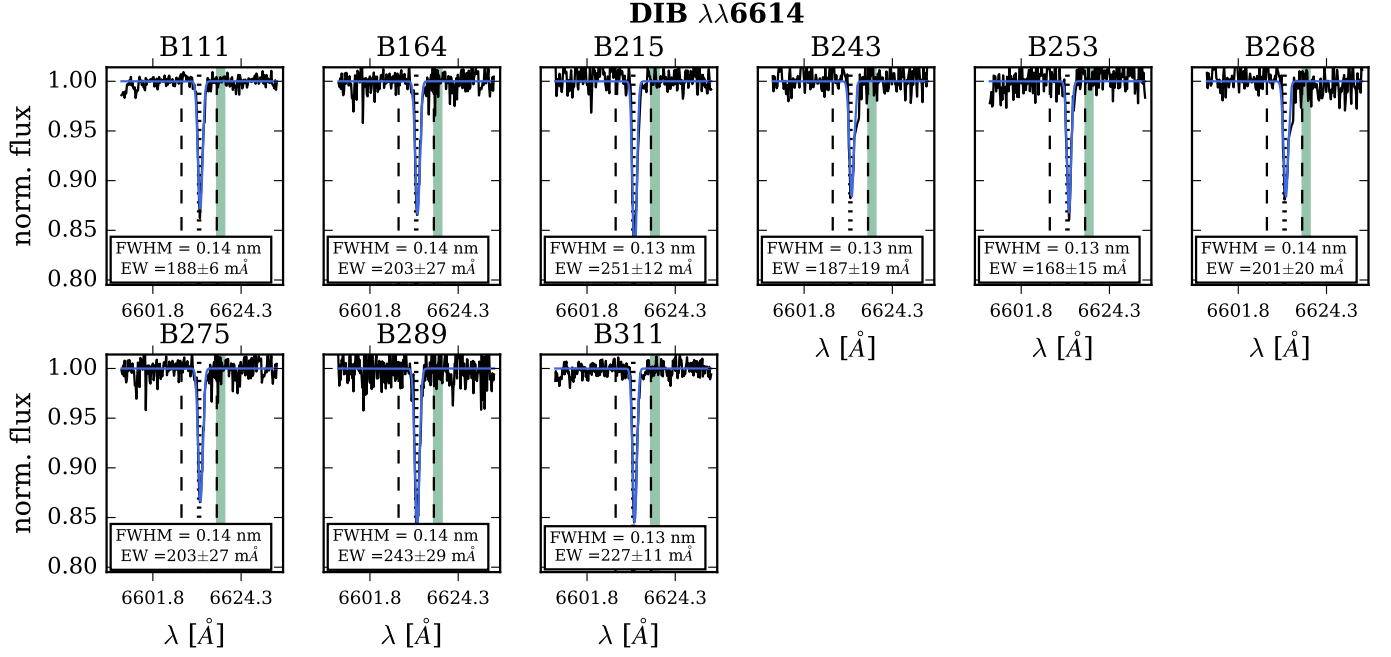


Fig. A.7. DIB profiles at 6614 Å. The vertical dashed lines show the integration limits used to calculate the DIB strength, the dotted line shows the central wavelength of the DIB, and the green shaded region shows the region in which the error was calculated. With a solid-blue line we show the Gaussian fit to the DIB profile. The white box in the bottom of each panel indicated the FWHM and EW of this DIB for each object.

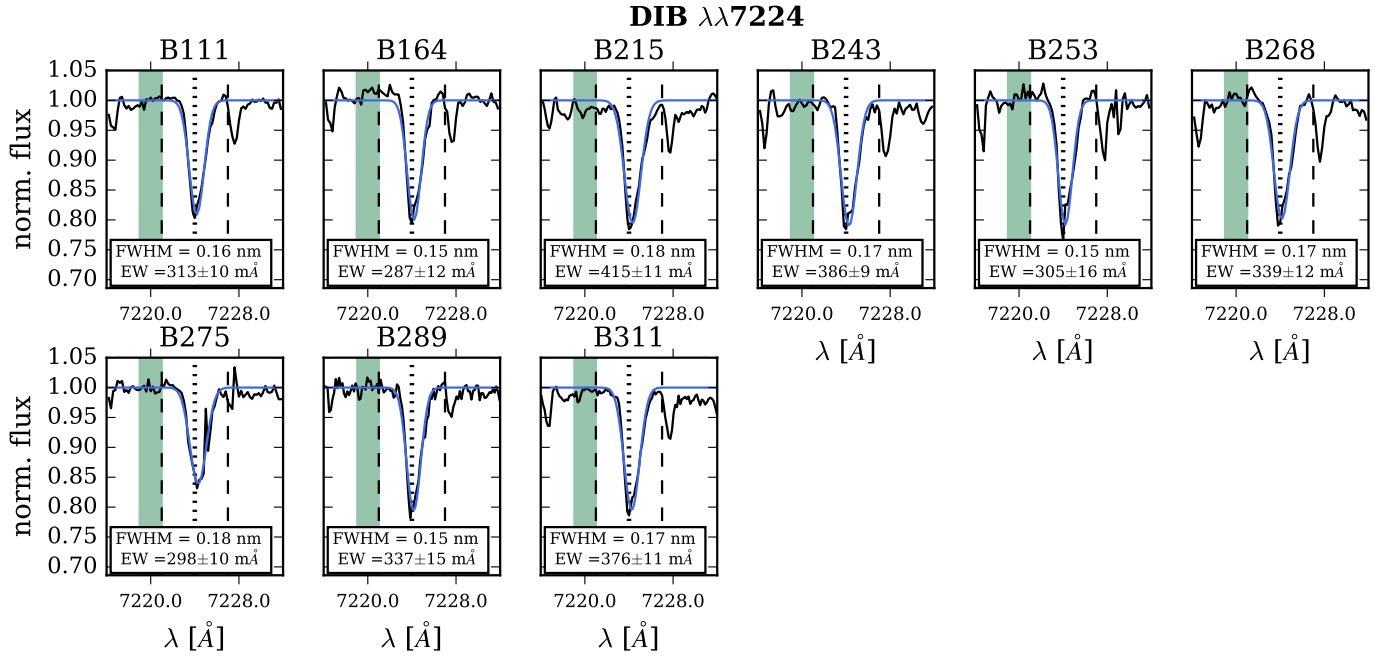


Fig. A.8. DIB profiles at 7224 Å. The vertical dashed lines show the integration limits used to calculate the DIB strength, the dotted line shows the central wavelength of the DIB, and the green shaded region shows the region in which the error was calculated. With a solid-blue line we show the Gaussian fit to the DIB profile. The white box in the bottom of each panel indicated the FWHM and EW of this DIB for each object.

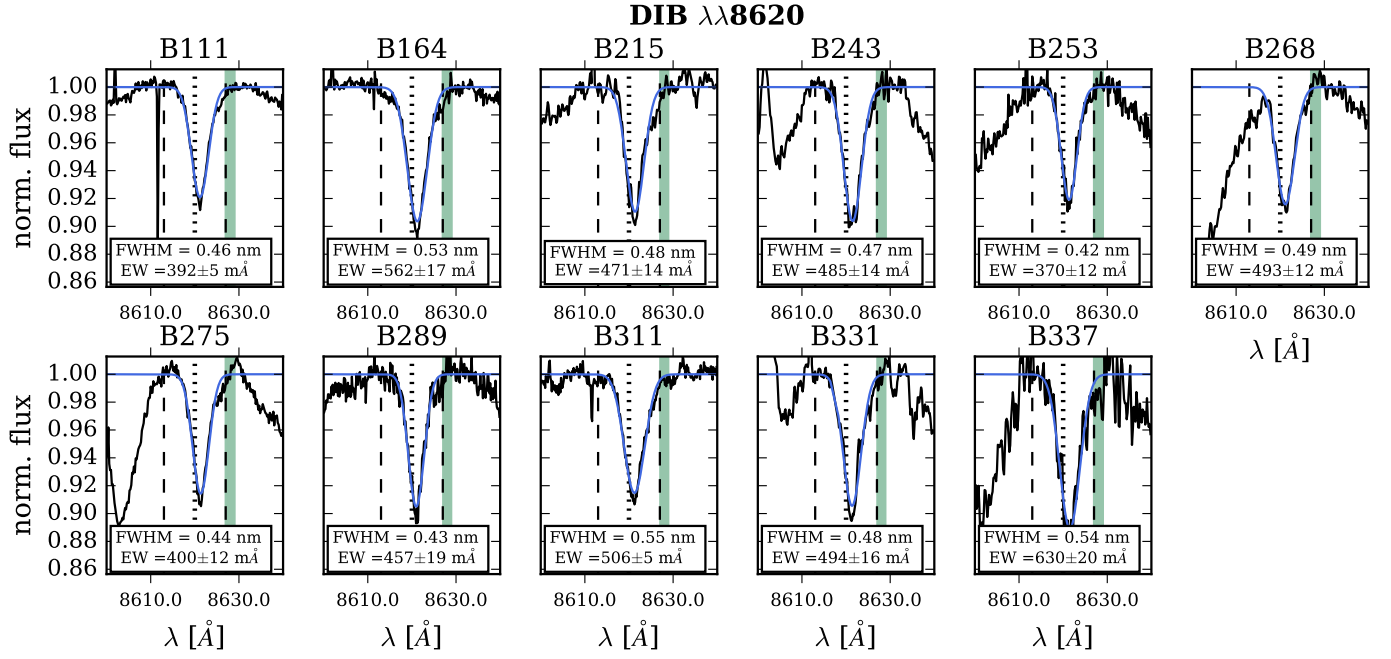


Fig. A.9. DIB profiles at 8620 Å. The vertical dashed lines show the integration limits used to calculate the DIB strength, the dotted line shows the central wavelength of the DIB, and the green shaded region shows the region in which the error was calculated. With a solid-blue line we show the Gaussian fit to the DIB profile. The white box in the bottom of each panel indicated the FWHM and EW of this DIB for each object.

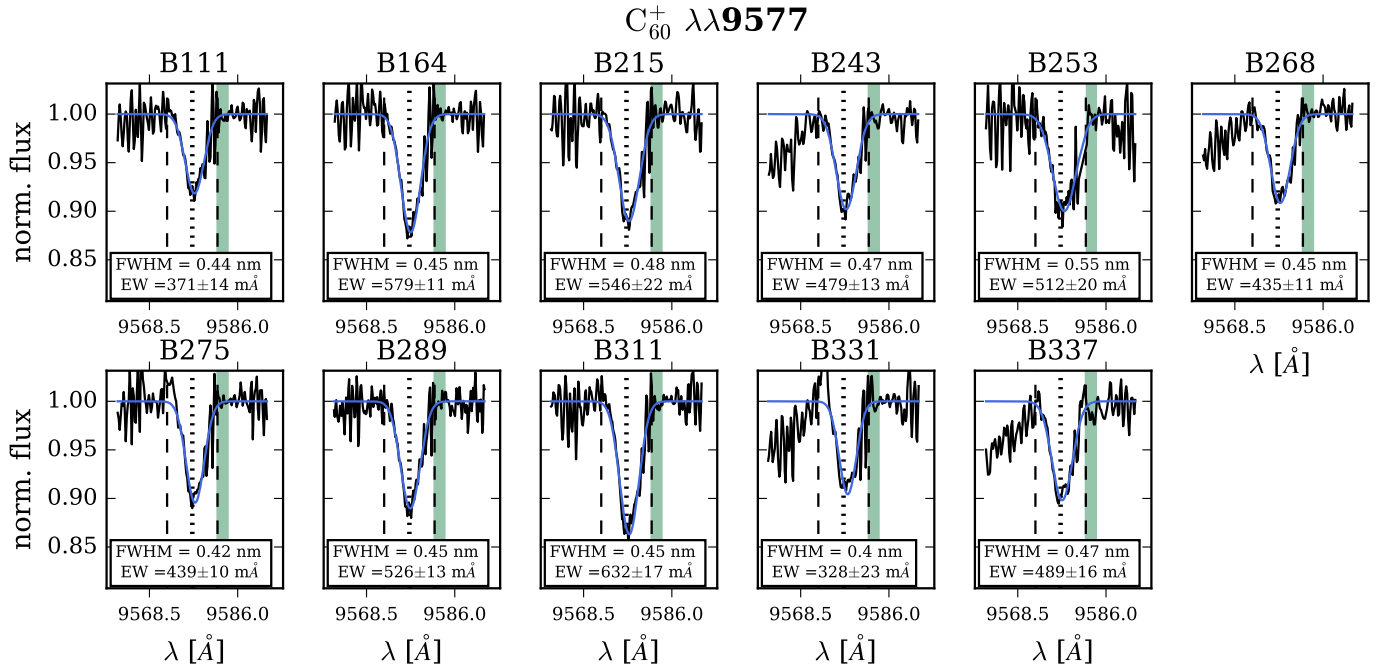


Fig. A.10. C₆₀⁺ DIB profiles at 9577 Å. The vertical dashed lines show the integration limits used to calculate the DIB strength, the dotted line shows the central wavelength of the DIB, and the green shaded region shows the region in which the error was calculated. With a solid-blue line we show the Gaussian fit to the DIB profile. The white box in the bottom of each panel indicated the FWHM and EW of this DIB for each object.

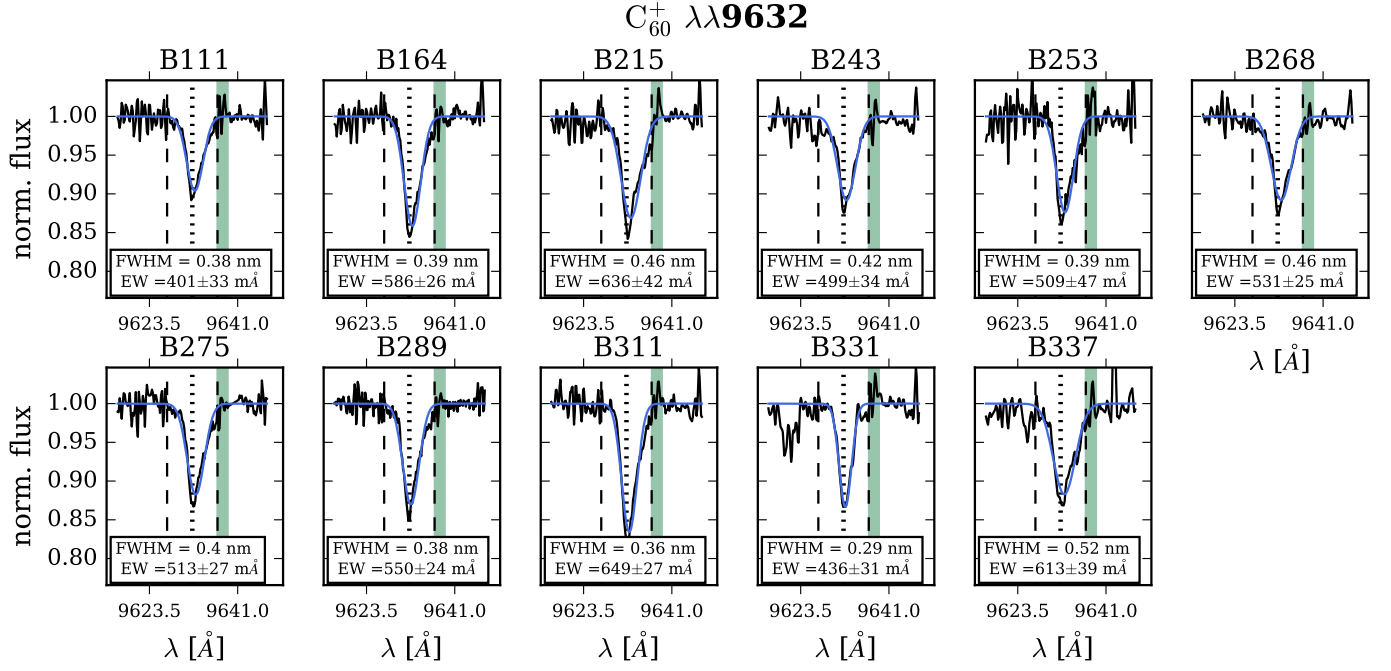


Fig. A.11. C_{60}^+ DIB profiles at 9632 Å. The vertical dashed lines show the integration limits used to calculate the DIB strength, the dotted line shows the central wavelength of the DIB, and the green shaded region shows the region in which the error was calculated. With a solid-blue line we show the Gaussian fit to the DIB profile. The white box in the bottom of each panel indicated the FWHM and EW of this DIB for each object.

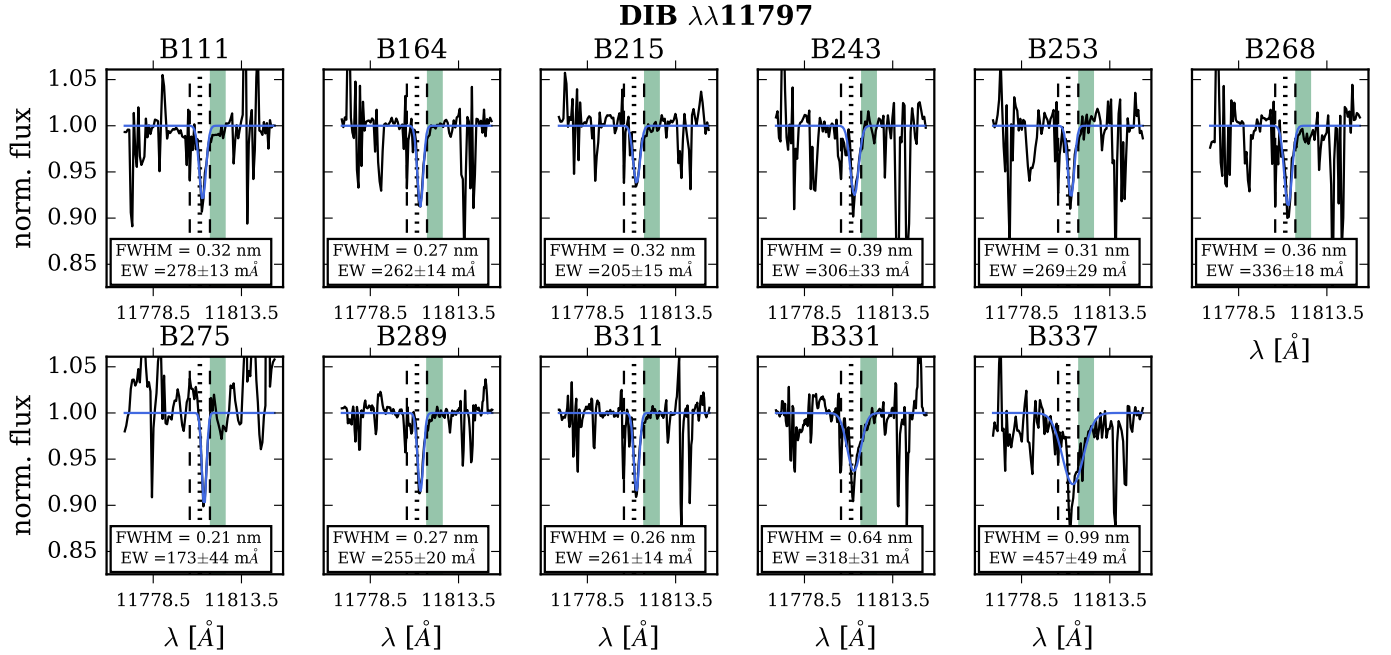


Fig. A.12. NIR DIB profiles at 11797 Å. The vertical dashed lines show the integration limits used to calculate the DIB strength, the dotted line shows the central wavelength of the DIB, and the green shaded region shows the region in which the error was calculated. With a solid-blue line we show the Gaussian fit to the DIB profile. The white box in the bottom of each panel indicated the FWHM and EW of this DIB for each object.

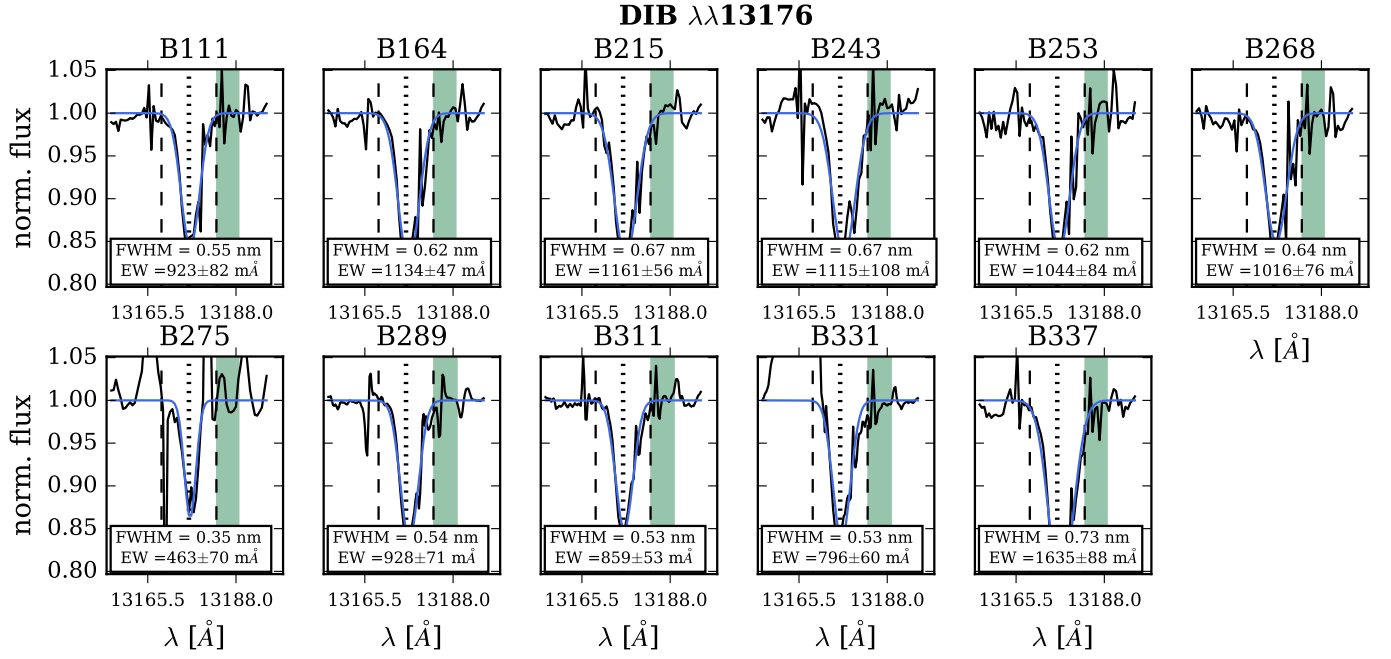


Fig. A.13. NIR DIB profiles at 13176 Å. The vertical dashed lines show the integration limits used to calculate the DIB strength, the dotted line shows the central wavelength of the DIB, and the green shaded region shows the region in which the error was calculated. With a solid-blue line we show the Gaussian fit to the DIB profile. The white box in the bottom of each panel indicated the FWHM and EW of this DIB for each object.

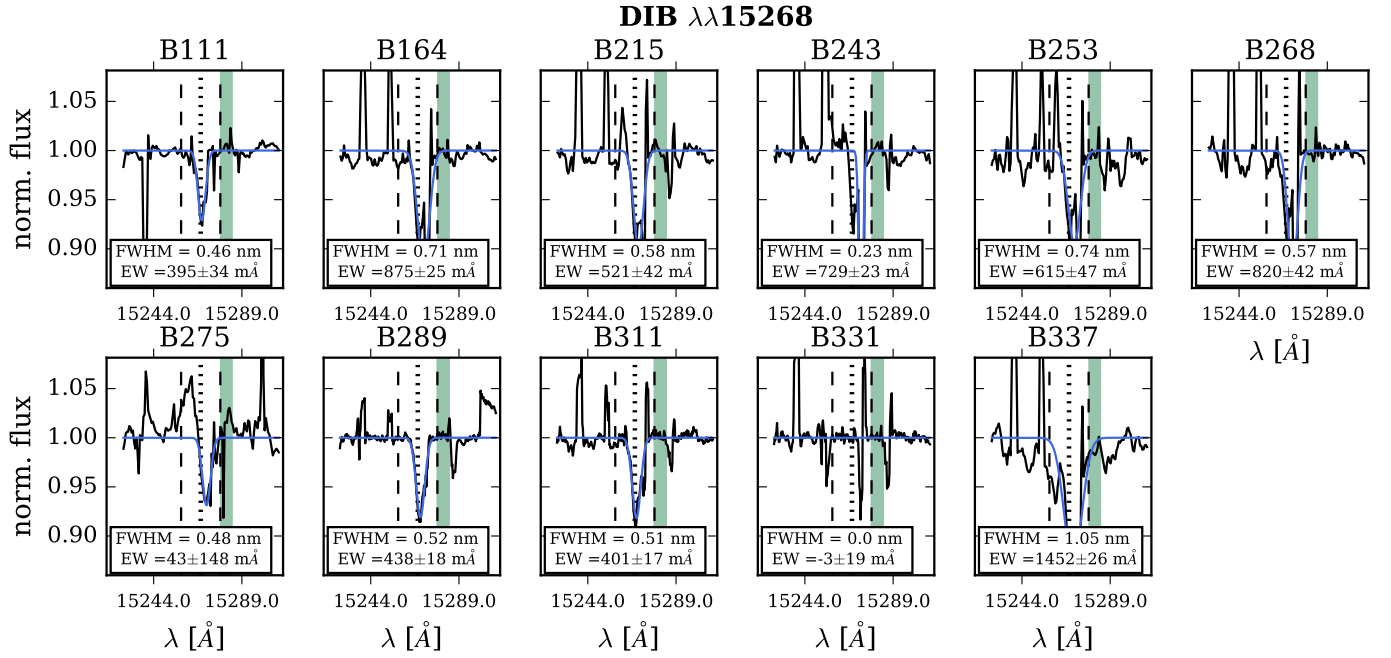


Fig. A.14. NIR DIB profiles at 15268 Å. The vertical dashed lines show the integration limits used to calculate the DIB strength, the dotted line shows the central wavelength of the DIB, and the green shaded region shows the region in which the error was calculated. With a solid-blue line we show the Gaussian fit to the DIB profile. The white box in the bottom of each panel indicated the FWHM and EW of this DIB for each object.